

MANIPULATION OF ELECTRICAL RESISTIVITY AND OPTICAL PROPERTIES  
OF ZINC OXIDE THIN FILMS GROWN BY PULSED LASER DEPOSITION AND  
THE SOL-GEL METHOD

by  
Ryan W. Crisp

A thesis submitted to the Faculty and the Board of Trustees of the Colorado School of Mines in partial fulfillment of the requirements for the degree of Master of Science (Applied Physics).

Golden, Colorado

Date \_\_\_\_\_

Signed: \_\_\_\_\_  
Ryan W. Crisp

Signed: \_\_\_\_\_  
Dr. Reuben T. Collins  
Thesis Advisor

Golden, Colorado

Date \_\_\_\_\_

Signed: \_\_\_\_\_  
Dr. Thomas E. Furtak  
Professor and Head  
Department of Physics

## ABSTRACT

Adjusting and optimizing the electrical resistivity and optical transparency of transparent conducting oxides (TCOs) is critically important to the quality of many solid state devices. In this work, the electrical and optical properties of zinc oxide thin films grown by the sol-gel method and by pulsed laser deposition are studied. A minimum electrical resistivity of  $5.7 \times 10^{-4} \Omega \cdot \text{cm}$  at an oxygen partial pressure of 0.01 mbar for room temperature (RT) growth by pulsed laser deposition (PLD) was achieved. This optimal film had a calculated transparency  $>90\%$  in the visible region. The measurement techniques used and a full exploration of the various growth parameters (growth temperature, ambient gas type, ambient gas pressure, and annealing treatments) are discussed. The optimized growth parameters were applied to create a TCO top contact to nanorod structures that are potentially useful as solar cell devices. The application of this optimized film offers future work possibilities to perfect a promising up and coming device.

## TABLE OF CONTENTS

ABSTRACT . . . . .	iii
LIST OF FIGURES . . . . .	vi
LIST OF TABLES . . . . .	viii
ACKNOWLEDGMENTS . . . . .	ix
CHAPTER 1 INTRODUCTION . . . . .	1
CHAPTER 2 EXPERIMENTAL PROCEDURES AND CHARACTERIZATION TECHNIQUES . . . . .	5
2.1 Growth Methods . . . . .	5
2.1.1 Pulsed Laser Deposition . . . . .	5
2.1.2 Sol-Gel Deposition Method . . . . .	10
2.2 Post-Growth Treatments . . . . .	11
2.3 Measurement Techniques . . . . .	12
2.3.1 Hall Measurements . . . . .	12
2.3.2 Ellipsometry . . . . .	16
2.3.3 Other Routine Measurements . . . . .	19
CHAPTER 3 RESULTS AND DISCUSSION . . . . .	21
3.1 Sol-gel – PLD Comparison . . . . .	21
3.2 Growth on GaAs Substrates . . . . .	23
3.2.1 Ambient Gas Series . . . . .	24
3.2.2 Growth Temperature Series . . . . .	30

3.2.3 Post-deposition Treatments . . . . .	37
3.3 Applications to Devices . . . . .	39
CHAPTER 4 CONCLUSIONS . . . . .	44
REFERENCES CITED . . . . .	47
APPENDIX - ELLIPSOMETRY MODELING AND PARAMETERS . . . . .	52

## LIST OF FIGURES

Figure 2.1	Diagram of the terrace-ledge-kink model. . . . .	8
Figure 2.2	PLD chamber set-up. . . . .	9
Figure 2.3	Diagram showing the shadow mask clamping the sample to the holder/heater block. . . . .	9
Figure 2.4	Hall effect measurement set-up. . . . .	13
Figure 2.5	Van der Pauw geometry used to measure the Hall effect. . . . .	15
Figure 2.6	Energy-band diagram for a metal-n-type semiconductor junction for (a) separate materials (b) and materials in contact. . . . .	15
Figure 2.7	Energy-band diagram for ohmic contact of metal-n-type semiconductor with a (a) positive bias (b) or negative bias. . . . .	16
Figure 2.8	Spectroscopic ellipsometry measurement geography . . . . .	17
Figure 3.1	SEM cross-section of a typical ZnO film on GaAs substrate with a thickness of approximately 124 nm showing the high quality film grown by PLD. . . . .	23
Figure 3.2	Resistivity (a) carrier concentration (b) and mobility (c) for the AZO films grown on GaAs substrates . . . . .	25
Figure 3.3	Root-mean-square surface roughness as a function of ambient oxygen pressure during growth as determined by AFM. . . . .	28
Figure 3.4	Calculated transmission from $T = \exp(-\alpha t)$ for AZO films grown at RT in the oxygen pressure indicated. . . . .	31
Figure 3.5	Schematic representation of the layers used to model the ellipsometric data. . . . .	31
Figure 3.6	Transmission calculated from absorption coefficient and extrapolating the model for the optimal film. . . . .	32

Figure 3.7	Transmission through film and glass substrate from UV-Vis-NIR spectrophotometry measurements and calculated transmission from n and k values determined with ellipsometry. . . . .	32
Figure 3.8	Calculated n and k values for lowest resistivity sample grown at RT in 0.01 mbar O <sub>2</sub> by PLD on GaAs. Note the sharp increase in k as the wavelength decreases showing the onset of band-to-band transitions and thus increased absorption in the films. . . . .	33
Figure 3.9	Resistivity (a), carrier concentration (b) and Hall mobility (c) as a function of temperature. . . . .	35
Figure 3.10	XRD $2\theta$ measurements as a function of growth temperature. . . . .	36
Figure 3.11	Grain size as a function of growth temperature calculated from the Scherrer formula for films grown in 0.01 mbar oxygen ambient. . . . .	36
Figure 3.12	Calculated transmission spectra of films deposited at different growth temperatures on GaAs substrates at 0.01 mbar O <sub>2</sub> partial pressure. . . . .	38
Figure 3.13	Resistivity, carrier concentration and Hall mobility as a function of ambient gas during post-deposition annealing at 300 C. The AZO films were deposited at RT in 0.01 mbar oxygen ambient gas. . . . .	39
Figure 3.14	Sparsely packed GaAs nanorods before ZnO deposition. . . . .	40
Figure 3.15	Densely packed GaAs nanorods before ZnO deposition. . . . .	40
Figure 3.16	Sparsely packed GaAs nanorods after ZnO deposition. . . . .	41
Figure 3.17	Densely packed GaAs nanorods after ZnO deposition. . . . .	42
Figure 3.18	SEM image showing the region where the ZnO shell at the base of the rod interfaces with the ZnO film on the surface of the GaAs substrate. . . . .	43
Figure A.1	Typical ellipsometry fitting results for Psi and Del of the optimised film. . . . .	53

## LIST OF TABLES

Table 1.1	Alternate TCO materials and possible dopants. . . . .	3
Table 3.1	Tabulated data comparing the resistivity, mobility, and carrier concentration between films grown using a sol-gel process and films deposited by PLD as a function of annealing temperature in forming gas atmosphere. . . . .	21
Table 3.2	Resistivity values for RT growth compared to literature reports also at RT including the process pressure, substrate, and transparency. . . . .	33
Table 3.3	Summary of the FWHM, lattice constant, and peak position determined from XRD measurements. . . . .	34
Table A.1	Summary of the parameters used to model the optimal film. . . . .	52

## ACKNOWLEDGMENTS

I would like to thank Christian Weigand for his help in making all of this work possible. The days and weeks we spent in the lab growing and characterizing films were some of the best weeks of my life. Our invaluable discussions and his unwavering commitment to finishing this study and publishing the results were key to completing this thesis. The two summers I spent working with him in Norway were crucial to my success and for that I am forever in his debt. He grew several of the samples discussed herein, performed many of the XRD measurements, and took several amazing SEM pictures and for that I thank him.

I would also like to thank my adviser Reuben Collins for his scientific mentoring as well as the personal and life advice he shared with me along the way. The often intense group meetings with him and Tom Furtak helped to keep me focused on the bigger picture and not to lose sight of the forest through the trees. I would also like to thank Helge Weman and Cecile Ladam for sponsoring and helping me during my stay in Norway; without their help none of this would have been possible. Dheeraj Dasa provided me with many GaAs nanorod samples throughout this work and so I would like to thank him for growing all those rods for me as well.

Many of my fellow graduate students helped to make this thesis a success. Thomas Brenner's acquisition of AFM data was very useful. Jason Stoke's aid in ellipsometry modelling and all the many hours of tutoring on this subject helped me understand more about this particular area of physics than any book I've read to date.

My parents unending support kept me going even when times were rough and for that I am forever grateful. I could not have asked for better parents.

Finally, I would like to thank my significant other, Jessica, for her many late-night coffee runs that kept me going on my not-infrequent all-nighters. She has always been there for me - unquestioning and unfaltering - for which I owe many thanks. Thank you to all the others

I may have left out, I appreciate all the help I've received from everyone and for everything. Funding for this project was provided by the Norwegian Research Council under Grant No. 182092/S10, the US National Science Foundation under Grants No. DMR-0606054 and DMR-0907409 as well as the Renewable Energy Materials Research Science and Engineering Center, thank you.

# CHAPTER 1

## INTRODUCTION

In the quest to obtain ever-better solid state devices, Zinc Oxide (ZnO) is actively researched for its potential application to solar cells, light emitting diodes, lasers, and optoelectronic devices in general among other things [1–3]. Here the term ‘better’ is somewhat ambiguous and could refer to physical properties like improved conductivity or transparency, or it could also refer to economical factors such as the materials cost or expensive deposition process. In today’s fast-paced economy, any improvements could potentially yield financial gains, making research and development critical to advancing the state-of-the-art.

In this thesis, interest in ZnO stems primarily from its use as a transparent conducting oxide (TCO), a material which is optically transparent in the visible spectrum while at the same time exhibiting sufficient electrical conductivity to act as a contact layer. TCOs are commonly used as conducting window layers in flat panel displays, light emitting diodes, and solar cells. Improvements in their conductivity, transparency, and/or cost could result in substantial benefits in many applications. The quality of ZnO thin films has seen continued improvement over the past few years as evidenced by a decrease in the achievable resistivity by an order of magnitude, whereas improvements in the resistivity of Sn-doped  $\text{In}_2\text{O}_3$  (ITO) have seemingly reached a limit [4]. Currently, however, ITO is still the most commonly used material for TCO applications because its electrical and optical properties are still better than the alternatives [5]. A low resistivity of  $7.2 \times 10^{-5} \Omega\text{-cm}$  with a high transparency of  $\sim 90\%$  has been achieved under research conditions [6] while the commercially available material is only slightly more resistive at around  $1 \times 10^{-4} \Omega\text{-cm}$  [4]. However, In is  $\frac{\$794987.81 \text{ per metric ton}}{\$3400.00 \text{ per metric ton}} = 233.8$  times more expensive than Zn [7]. Furthermore, the prospects of reducing this cost difference are rather bleak since Zn is  $\frac{70 \text{ mg/kg}}{0.25 \text{ mg/kg}} = 280$  times more abundant than In in the Earth’s crust [8]. In light of these differences in the cost and availability of In to Zn, a switch

from indium-based TCOs to zinc-based TCOs could reduce costs and yield better devices assuming the electrical and optical properties of ZnO become more comparable to those of ITO. This comparison is between the two figures of merit for a TCO: the resistivity and the transparency. A list of TCO alternatives qualitatively ranking the resistivity of each is shown in Table 1.1 as well as the toxicity which can be an important factor as well. Furthermore, at a wavelength of 500 nm (roughly the middle of the visible spectrum, near the sun’s peak wavelength) the index of refraction for GaAs (a material widely used for high-efficiency solar cells and is studied herein) is  $n_{GaAs} = 4.3$  [9] and the index of refraction for ZnO is  $n_{ZnO} = 1.9$  (from ellipsometry modelling in this work) meaning that the reflectance, from  $R = \frac{(n_{ZnO} - n_{GaAs})^2}{(n_{ZnO} + n_{GaAs})^2}$ , is minimized when the index of ZnO is roughly  $\sqrt{n_{GaAs}}$  which is around 2.07 at this wavelength [10]. By adding a layer between the between the air/GaAs interface that is at an index value between the two, this layer acts like a graded interface and “eases” the transition of the light into the GaAs. Because the indices are approximately matched at this ideal value, the ZnO makes an anti-reflection coating and is thus an optimal material to use for a TCO. All things considered, Al-doped ZnO seems to be the most promising candidate to date but work is being done on many other host materials and dopants as well in an effort to improve TCO performance, indicating that this is a very active research area.

It is the purpose of this thesis to demonstrate the ability to manipulate the electrical resistivity and optical properties of ZnO thin films by doping, annealing, and altering the growth conditions to meet the goal of creating a TCO for particular GaAs-based devices. First, a comparison of different deposition methods is performed and the effects of annealing in a reducing atmosphere and doping are explored. The sol-gel method, an inexpensive and simple technique, is used in this comparison study to develop the process parameters and measurement techniques for making and testing TCOs. Applying the results of the comparison study to potential devices and extending the work further, the effects of total pressure, ambient gas type, growth temperature, and post-growth annealing on the electrical, structural, and optical properties of Al-doped ZnO (AZO) grown on GaAs substrates by

Table 1.1: Alternate TCO materials and possible dopants. From [5].

Binary	Dopant	Resistivity	Toxicity
ZnO	Al, Ga, B, In, Y, Sc, V, Si, Ge, Ti, Zr, Hf, // F	⊙	
CdO	In, Sn	⊙	××
In <sub>2</sub> O <sub>3</sub>	Sn, Ge, Mo, Ti, Zr, Hf, Nb, Ta, W, Te // F	⊙	×
Ga <sub>2</sub> O <sub>3</sub>	Sn	Δ	
SnO <sub>2</sub>	Sb, As, Nb, Ta // F	○	
TiO <sub>2</sub>	Nb, Ta	Δ	
Temary			
MgIn <sub>2</sub> O <sub>4</sub>		Δ	
GaInO <sub>3</sub> , (Ga, In) <sub>2</sub> O <sub>3</sub>	Sn, Ge	Δ	
CdSb <sub>2</sub> O <sub>6</sub>	Y	Δ	×
SrTiO <sub>3</sub>	Nb, La	×	
Temary			
Zn <sub>2</sub> In <sub>2</sub> O <sub>5</sub> , Zn <sub>3</sub> In <sub>2</sub> O <sub>6</sub>	Multi-component ZnO–In <sub>2</sub> O <sub>3</sub> system	○	
In <sub>4</sub> Sn <sub>3</sub> O <sub>12</sub>	In <sub>2</sub> O <sub>3</sub> –SnO <sub>2</sub> system	○	
CdIn <sub>2</sub> O <sub>4</sub>	CdO–In <sub>2</sub> O <sub>3</sub> system	○	×
Cd <sub>2</sub> SnO <sub>4</sub> , CdSnO <sub>3</sub>	CdO–SnO <sub>2</sub> system	○	×
Zn <sub>2</sub> SnO <sub>4</sub> , ZnSnO <sub>3</sub>	ZnO–SnO <sub>2</sub> system	Δ	
	ZnO–In <sub>2</sub> O <sub>3</sub> –SnO <sub>2</sub> system	○	
	CdO–In <sub>2</sub> O <sub>3</sub> –SnO <sub>2</sub> system	○	×
	ZnO–CdO–In <sub>2</sub> O <sub>3</sub> –SnO <sub>2</sub> system	○	×

: ⊙Very good, ○: Good, Δ: Average, ×: Bad, ××: Very bad.

pulsed laser deposition are analyzed. Despite widespread interest in both ZnO and GaAs, to the best of my knowledge, there has not been a thorough examination of the effects of growth ambient and temperature effects of AZO grown on GaAs substrates using pulsed laser deposition. Singh *et al.* also note the apparent lack of documentation of these effects [11]. The final product of this work is an optimized room temperature (RT) deposited TCO for use on GaAs-based devices. This project enhances the work done within Helge Weman's research group at Norwegian University of Science and Technology and works towards creating a GaAs nanorod-based solar cell. Preliminary work growing conformal TCO top contacts on GaAs nanorod solar cells is presented. While the growth and characteristics of the rods are not presented here, a more complete description can be found at [12].

## CHAPTER 2

### EXPERIMENTAL PROCEDURES AND CHARACTERIZATION TECHNIQUES

This chapter is devoted to describing the processes used to grow the films, the post-deposition treatments, and also the methods used to characterize the films, including the underlying theories behind them.

#### 2.1 Growth Methods

There are many methods used to grow ZnO thin films including sputtering, atomic layer deposition, chemical vapor deposition, thermal evaporations, dip coating, and so forth. The two methods explored herein are pulsed laser deposition (PLD) and the sol-gel method by varying the doping, annealing conditions, and growth ambient.

##### 2.1.1 Pulsed Laser Deposition

The PLD process utilizes laser-light incident on some target material to eject energetic species in what's known as a plume from the bulk material. In order to generate a plume, the incident electromagnetic field on the target given in Eq. 2.1 must be intense enough to cause dielectric breakdown to generate the plasma constituting the plume [13]. According to Willmott [13] ablation of the target material is dependent on the thermal conduction through the target with a thermal diffusion depth of  $l = 2\sqrt{D\tau}$  where  $D$  is the diffusion coefficient and  $\tau$  is the characteristic time during which this process occurs. When the laser pulse has a duration much shorter than the characteristic time it takes to couple the energy from the electrons to the lattice, then ablation occurs without 'collateral' damage or heating of the target[13]. Starting with the electric field amplitude that will generate the plume, given by [14]

$$E = \left( \frac{2u_{EM}}{n\epsilon_0} \right)^{1/2} \quad (2.1)$$

where  $u_{EM}$  is the energy density,  $n$  is the refractive index of the target material, and  $\epsilon_0$  is the permittivity of free space. There is some threshold laser fluence (related to the energy density) that is dependent on the optical absorption coefficient,  $\alpha$ , and the pulse duration, where sufficient energy has been absorbed by the target substrate to cause evaporation and ionization and a plasma plume is ejected. This plume travels outwards and condenses on the sample surface thus growing a film. The energy of the species in the plume are typically high enough to allow for surface mobility once the constituents reach the sample substrate while still having an energy low enough to not damage the surface upon impact [13].

Once the species condense on the surface they have a certain surface mobility dependant on the energy imparted to the species from the laser and the system temperature. Under certain conditions they are able to crystallize or they will form an amorphous film assuming they are not devolved completely from the surface. The terrace-ledge-kink model is one way of describing crystal surfaces in which the adatoms (the ‘building blocks’ of the crystal) are represented as cubes that can be deposited in a number of different positions, each with an associated energy, on the crystal surface [15]. The different positions the adatoms can occupy is shown in Figure 2.1. Each block in the model can be bonded with up to 6 nearest neighbors, so removing or placing a block can lower or raise the Gibbs free energy of the system by a maximum of 6 bond-energy units [16]. In terms of the change in Gibbs free energy, ledges and kinks are energetically preferred to surface sites because the energy of the system is minimized as shown in Eq. 2.2, which encourages crystalline growth in the system. The energy change to go from a surface state to a kink site is [15]

$$\Delta G = W_f - W_i \tag{2.2}$$

where  $W_f$  and  $W_i$  are the final and initial bond energies so to move from a surface cite to a kink site we have 3 bonds - 1 bond = 2 bonds created resulting in a reduction in the potential energy by 2 bond-energy-units.

However, many of the films grown in this study were deposited at room temperature meaning that once the growth species have equilibrated with the surface the thermal energy

available to break and reform bonds is on the order of  $kT = 0.0259$  eV. At this low energy, reorganization from an adatom's original deposition position to one that enhances the crystallinity is not very likely because the number of atoms undergoing a transition,  $n$ , depends on the temperature  $T$ , number of available atoms  $N$ , and the change in Gibbs free energy  $\Delta G$  given by [16]

$$n = N \exp\left(\frac{-\Delta G}{kT}\right). \quad (2.3)$$

For a certain value of  $\Delta G$ , increasing the energy,  $kT$ , would increase the amount of atoms able to reorganize to a more energetically favorable position (i.e. minimizing the energy of the system). During deposition, the species in the plume gain energy from the laser pulse that they carry with them to the substrate. This energy allows a greater number of atoms to reorganize before equilibrating and is a function of the ambient pressure, it effectively increase the plume species temperature. In the low pressure regime ( $p < 0.001$  mbar) the Knudsen number is given by [17]

$$Kn = \frac{l}{L} \quad (2.4)$$

where  $l$  is the mean free path and  $L$  is the characteristic dimension for the process (in this case the target-to-substrate distance). For this regime  $Kn > 1$  (estimating that the particle size is 0.3 nm so  $l \approx 10$  cm [17]) meaning the mean free path of the particles composing the plume is larger than the target-substrate distance so the particles do not lose any energy due to collisions before arriving at the substrate. On the other hand, in the high pressure regime ( $p > 0.1$  mbar) the  $Kn < 0.01$  meaning we are in a fluid flow process regime where there are many collisions between the plume species and ambient gas resulting in a reduction in energy that the particles have when they reach the sample surface.

While the terrace-ledge-kink model describes the structure and energetics of crystal surfaces, there are three main modes for actually growing thin films: Volmer-Weber growth, Frank-van der Merwe growth, and Stranski-Krastanov growth [18]. Volmer-Weber growth is characterized by island formation of adatoms which nucleate and grow 3 dimensionally until

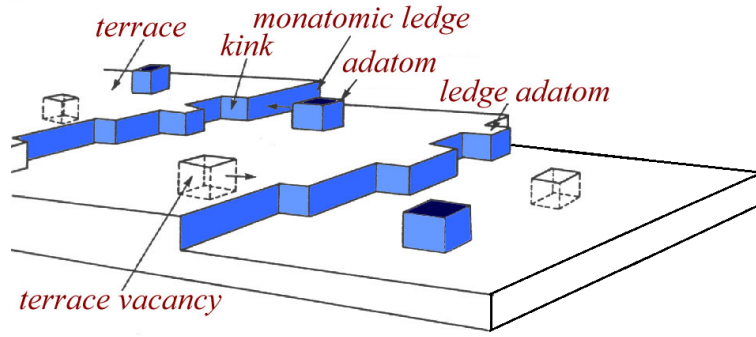


Figure 2.1: Diagram of the terrace-ledge-kink model. Modified from [15].

they coalesce into a film. Opposite the spectrum from the island growth mode is Frank-van der Merwe growth by which films are formed one monolayer at a time as the adatoms are more likely to wet the surface than to clump together. Stranski-Krastanov growth is then an intermediate between the two others where film growth is layer-by-layer at first then transitions into island growth after the first few monolayers. The particular growth mode that occurs is dependent on the surface energetics of the vapor, substrate, and film. For the materials used in this study, Volmer-Weber growth is the most likely growth mode for these semiconductor-semiconductor type systems explored herein [16].

The PLD set-up used in this study is shown schematically in Figure 2.2. The films were deposited using a 248 nm KrF excimer laser (Lambda Physik 210i) to ablate a ZnO target doped at 2.0 wt.% Al (99.999%, American Elements Inc.). The laser made a 15 mm diameter raster pattern on the target. The on-axis deposition occurred at a 45 mm target-to-substrate distance. The calculated energy density on target is 1.1 - 1.6 J/cm<sup>2</sup>. Deposition time (based on number of pulses at a 10 Hz repetition rate) was adjusted to obtain 100 ± 20 nm thick films. I used a square 5 mm x 5 mm shadow mask to precisely control the area of the films being deposited and also firmly affix the sample substrate to the heater block by sandwiching the sample substrate between the heater and the mask (See Figure 2.3).

The substrate temperature varied from room temperature (RT) to 500 C. The GaAs (111)B and glass substrates used were heated by a resistive heating element and the tem-

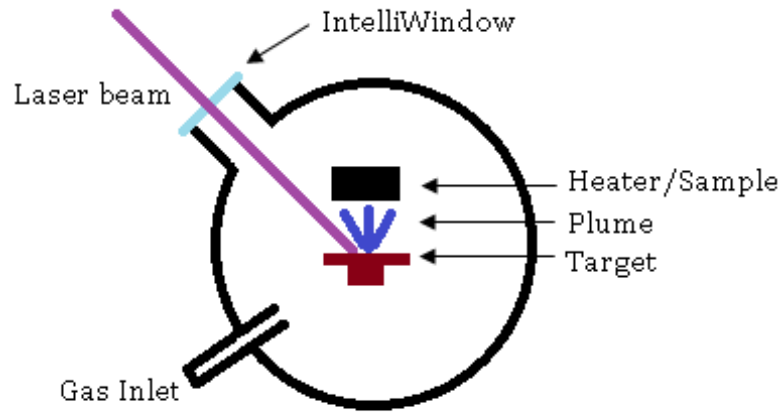


Figure 2.2: PLD chamber set-up.

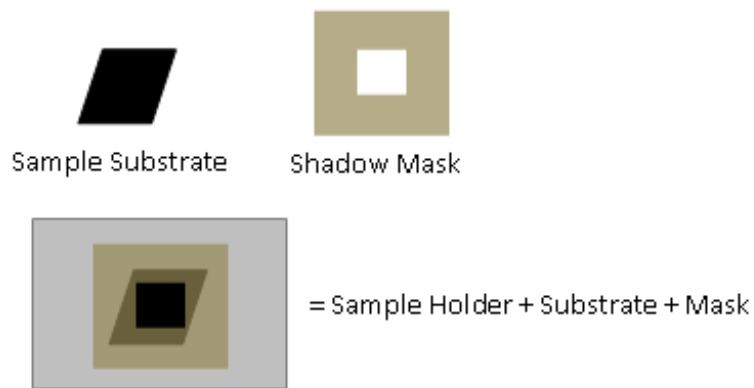


Figure 2.3: Diagram showing the shadow mask clamping the sample to the holder/heater block.

perature was redundantly measured using a thermocouple attached to the heater block and using an IR optical thermometer to measure the substrate directly. Temperature readings were taken in the center, on the left-, and right-side of the sample to verify uniform heating of the substrate. If the target was removed from the deposition chamber or was used for longer depositions ( $>60$  min), it was polished with 1200-grit sandpaper and pre-ablated at a rate of 5 Hz for 20 minutes to have a clean fresh surface before depositing.

### 2.1.2 Sol-Gel Deposition Method

A Sol-gel process is a wet chemical deposition method that is relatively inexpensive because complicated equipment is not needed, the chemical precursors (at least for ZnO) are inexpensive and not environmentally hazardous, and the energy input is typically minimal [19]. Film growth using a sol-gel process is different from that of PLD. The solution is often spin-coated onto the sample substrate and then a heat treatment is performed where the matrix that the Zn is suspended in decomposes while the Zn oxidizes to form a dense ZnO thin film [19]. Often this process is repeated in order to build up thick films because each step only deposits 20-50 nm. For the films in this study I first followed the procedure outlined by Ohyama [20] where a chemical solution prepared with 0.826 g zinc acetate dihydrate, 0.233 mL ethanolamine, and 5 mL 2-methoxy-ethanol is stirred on a hot plate at 60 C for 30 min. Next, the solution is dispensed on a glass substrate (soda-lime glass microscope slide) and spin-coated at 2000 rpm for 60 seconds. The films were then dried at 300 C for 10 minutes and cooled with a heat sink before repeating the process for a total of 7 layers. Unfortunately, these films were too resistive for Hall measurements. However, there are several methods reported in the literature for making more conductive films. One such experiment doped the zinc oxide films with silver [21]. A further experiment annealed the films in a furnace with a 5%-95% mixture of hydrogen to nitrogen at various temperatures [22]. A third experiment by Yao *et al.* introduced aluminum chloride in the precursor solution to dope the films while in the aqueous phase before annealing in H<sub>2</sub>, which resulted in a resistivity of  $9.90 \times 10^{-3} \Omega\cdot\text{cm}$  [23]. I combined the procedures of Lee and Yao in order to

make the films more conducting by both doping the films and performing heat treatments. I added to the sol-gel solution described above 0.0204 g of aluminum chloride hexahydrate to obtain a 2.25 at.% ratio of Al to Zn, roughly the same doping concentration as used in the PLD grown films. I deposited 7 layers one at a time according to the procedure described above, except I lowered the spin speed to 800 rpm (Yao used 1000 rpm [23]) to maximize film thickness while still allowing the sol-gel solution (now including aluminum chloride) to dry without blistering. Once the last drying heat treatment was performed, I annealed the films in H as described in Section 2.2.

## 2.2 Post-Growth Treatments

Samples grown on GaAs using PLD were annealed *in-situ* at various temperatures ranging from 300 C to 500 C and in two ambient gases (O<sub>2</sub> and Ar) and at various pressures ranging from vacuum (10<sup>-7</sup> mbar) to 0.5 mbar for 1 hour. Oxygen was used to examine the effects of doping through oxygen vacancies (or lack thereof) with Argon being used as a control for pressure effects in addition to its use for inducing oxygen vacancies perhaps by not compensating for an initially non-stoichiometric plume. After finishing the deposition, the PLD chamber was pumped down before starting the gas flows of O<sub>2</sub> or Ar. The sample was not removed from the chamber until after the anneal. Once an hour was up the heater and gas flows were turned off and once the sample was cool, it was removed from the chamber.

The hydrogen anneal, on the other hand, was performed in a quartz tube furnace for 1 hour in a reducing atmosphere of 2.9/96.1% by volume H<sub>2</sub>/Ar mixture at a flow rate of 1.75 lpm. This portion of the study focuses on the temperature range of 400 C to 600 C. Hydrogen could either serve as a dopant or fill vacancies thus removing doping so the role it plays is worth investigating for these films.

All samples grown on glass using PLD or a sol-gel process only received a H/Ar anneal. PLD-grown samples on GaAs were treated with all three annealing ambient gases.

The effects of annealing in a reducing atmosphere of hydrogen have been reported in literature for sol-gel films [22–24]. Often defects in the material can be ‘annealed out’ in

a process known as point defect healing [25]. Increasing the crystal quality increases the time between scattering events,  $\tau_s$ , thus reducing the resistivity of the sample. Grain size increases reduce the grain boundary scattering of charge carriers leading to more conductive films as well [26, 27]. Not only does annealing increase the conductivity, it can also increase the transparency of the film by reducing the number of mid-band gap defect states that allow sub-band gap light to be absorbed [28]. Furthermore, the absorption edge at the band gap tends to sharpen and thus increase the ‘window’ in the spectrum where the films are transparent which will be discussed more later.

## 2.3 Measurement Techniques

Here I will give the theory and discuss the techniques used to measure the physical properties explored in this study.

### 2.3.1 Hall Measurements

Hall effect measurements are at the crux of this thesis as several of the semiconductor’s properties can be determined from this one measurement, including the carrier concentration, carrier type, and mobility. The Hall effect arises from the balancing of the electric force and the magnetic (Lorentz) force acting upon the moving charges present in the semiconductor. When a current, denoted by  $I_x$  in Figure 2.4, passes through the sample placed in a uniform magnetic field,  $B_z$ , the electrons in an  $n$ -type material (or holes in a  $p$ -type material) experience a force (the Lorentz force) given by [29]

$$\vec{F} = q\vec{v} \times \vec{B} = qv_x B_z \hat{y} \quad (2.5)$$

where  $q = -1.602 \times 10^{-19}$  C is the electronic charge,  $v_x$  is the drift velocity in the x-direction, and  $B_z$  is the z-component of the magnetic field. At some point the system will be in steady-state where the electric field caused by the electrons ‘building up’ at one side balances the Lorentz force yielding the relation

$$qE_y = qv_x B_z \quad (2.6)$$

where the electric field,  $E_y$ , produces a voltage,  $V_H = E_y W$ , known as the *Hall voltage* [29]. An illustration of the Hall effect is shown in Figure 2.4.

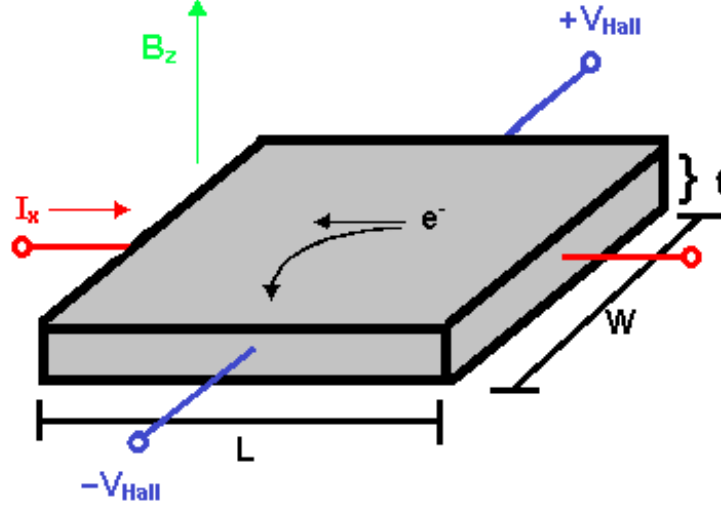


Figure 2.4: Hall effect measurement set-up.

Assuming that the majority carrier concentration (electrons in the case of *n*-type ZnO) is much larger than the minority carrier concentration,  $n \gg p$ , we can write the drift velocity as

$$v_{drift,x} = -\frac{J_x}{en} \quad (2.7)$$

where  $J_x$  is the current density in the x-direction,  $e$  is the electron charge, and  $n$  is the electron concentration. Then combining Equation(2.7) and Equation(2.6) the Hall voltage can be expressed as

$$V_H = -\frac{I_x B_z}{ent} \quad (2.8)$$

with  $t$  being the thickness of the sample. By applying the following conditions from van der Pauw [30], a sample's resistivity, doping type, sheet carrier density, and mobility can be calculated from the Hall effect using a set-up known as the van der Pauw geometry. The conditions are:

- The contacts are at the circumference of the sample.

- The contacts are sufficiently small.
- The sample is homogeneous in thickness.
- The sample does not have isolated holes.

With the van der Pauw geometry shown in Figure 2.5, resistivity and Hall measurements were taken using a Lakeshore 7504 Hall measurement system for the films grown in the GaAs substrate study. Ohmic contacts for the study of AZO growth on GaAs were e-beam evaporated onto the corners of the sample using a shadow mask to isolate each contact. The contacts consist of a 20 nm Ti adhesion layer capped off by 150 nm of Au to protect the Ti from oxidation and provide a low resistance, mechanically robust pad to place the Hall probe contacts. This Ti/Au layered contact structure is reported by Lee *et al.* to have a low specific contact resistance of  $7.3 \times 10^{-3} \Omega \cdot \text{cm}^2$  for moderately doped films ( $n = 7 \times 10^{17} \text{ cm}^{-3}$ ) [31] whereas Ip *et al.* reports a specific contact resistance of  $8 \times 10^{-7} \Omega \cdot \text{cm}^2$  for more heavily doped films where  $n = 1.5 \times 10^{20} \text{ cm}^{-3}$  [32]. With the typical contact size on the sample being  $7.5 \times 10^{-3} \text{ cm}^2$ , with the carrier concentrations used in this study all roughly in the range  $10^{17} - 10^{20}$ , and the linear I-V curves taken before Hall measurements, the contacts are ohmic and have negligible contact resistance:  $R_c < 2 \Omega$  so compared to  $60 \Omega$  for the film with the lowest resistance it is indeed negligible. Kim *et al.* [33] argue that the ohmic nature of Ti/Au on ZnO is caused by the formation of a thin Ti - O interface layer. They reason this interface layer is created by Ti inducing the ‘out-diffusion’ of O from the ZnO bulk thus causing an increase in the n-type defect doping of the ZnO from oxygen vacancies at the metal-semiconductor interface. The active and preferential reaction of Ti with O is attributable to the significantly lower enthalpy of formation of  $\text{TiO}_2$  and  $\text{TiO}$  compared to that of ZnO ( $\Delta H_{\text{TiO}_2} = -944 \text{ kJ/mol}$  and  $\Delta H_{\text{TiO}} = -519 \text{ kJ/mol}$  compared to  $\Delta H_{\text{ZnO}} = -350 \text{ kJ/mol}$ ) [34].

The samples in the comparison study between PLD and sol-gel prepared films on glass substrates were all measured on a Bio-Rad Hall Effect Machine that uses a 0.4 T permanent

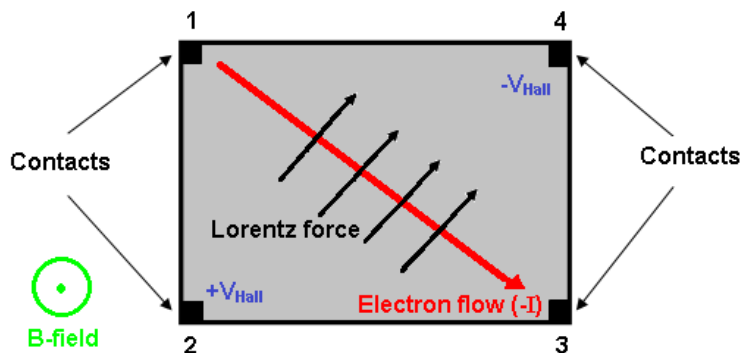


Figure 2.5: Van der Pauw geometry used to measure the Hall effect.

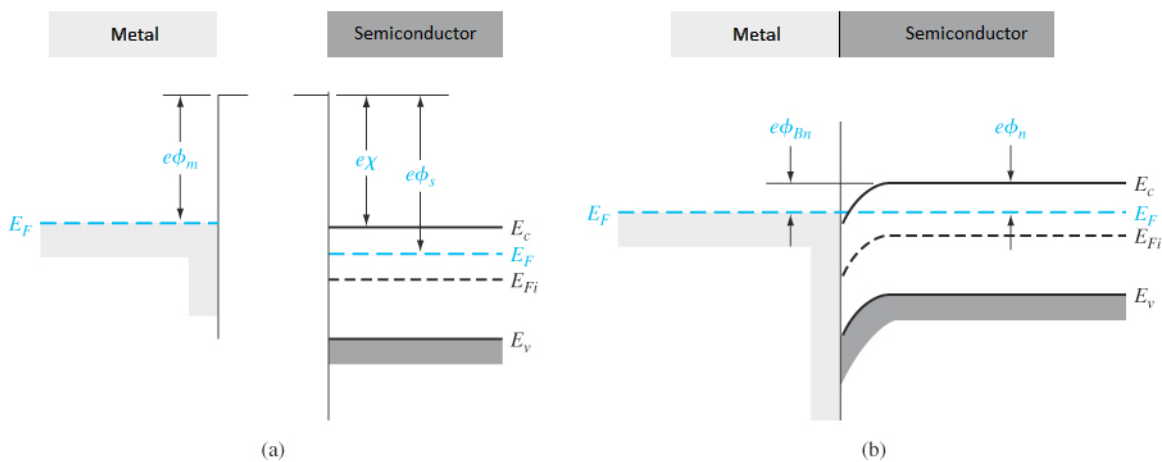


Figure 2.6: Energy-band diagram for a metal-n-type semiconductor junction for (a) separate materials (b) and materials in contact. From [29].

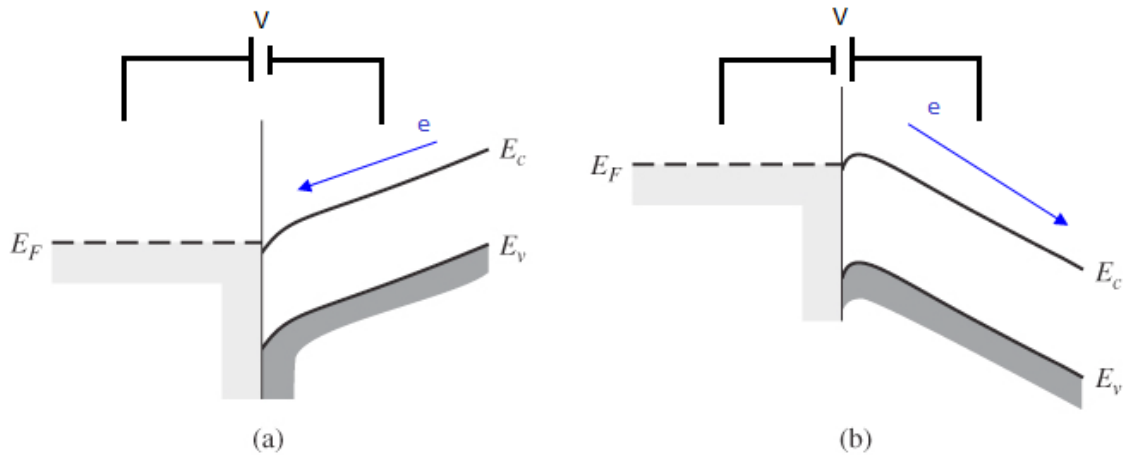


Figure 2.7: Energy-band diagram for ohmic contact of metal-n-type semiconductor with a (a) positive bias (b) or negative bias. Modified from [29].

magnet to induce the Hall effect. These films were contacted by soldering In to the corners of the samples. Indium, like Ti/Au, also provides an ohmic contact to ZnO [35]. With In's work function of 4.12 eV [36] and a typical work function for ZnO of 5 eV [37], the resulting energy-band diagram is shown in Figure 2.6 and leads to an Ohmic contact between the metal and the semiconductor because there is no potential barrier that the electrons have to surmount. In energy-band diagrams electrons will naturally travel 'downhill' where band bending occurs. Therefore when a positive or negative bias is applied across the junction the bands will bend as shown in Figure 2.7 and the electrons will flow without impedance by any barrier.

### 2.3.2 Ellipsometry

Ellipsometry is a very sensitive optical characterization technique that measures the change in polarization state after an incident light beam interacts with a sample [38]. Figure 2.8 shows the geometry used to take spectroscopic ellipsometry measurements.

The light beam begins in a known linearly polarized state, reflects off the sample, and is picked up by the detector which measures  $\psi$  and  $\Delta$ , two quantities related to the change in

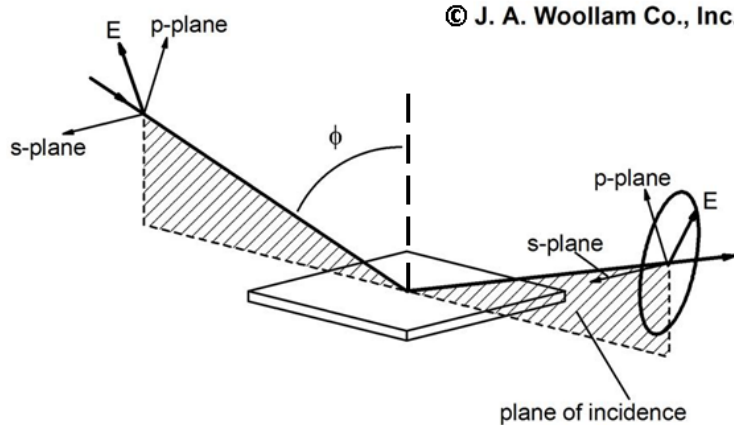


Figure 2.8: Spectroscopic ellipsometry measurement geography showing how the p-plane is parallel and s-plane is perpendicular to the incident plane. From [38]

polarization state  $\rho$  given by [38]

$$\rho = \frac{R_p}{R_s} = \tan(\psi)e^{i\Delta} \quad (2.9)$$

where  $R_p$  and  $R_s$  are the complex Fresnel reflection coefficients for light polarized in the p-direction and the s-direction, respectively. For light polarized in the p-direction, the electric field intensity vector lies in the plane parallel to the plane of incidence as shown in Figure 2.8. The s-direction is perpendicular to the p-direction such that the p-, s-, and propagation direction form a right-handed coordinate system [38].

Spectroscopic ellipsometry (SE) measurements using a J. A. Woollam Co. VASE rotating analyser ellipsometer were performed on selected samples in this study in the range of 360 nm to 1300 nm at a  $70^\circ$  angle of incidence. The GaAs wafers used were double-side polished. To help alleviate the potential modelling difficulties caused by incoherent reflections from the highly reflective backside of the wafer, clear Scotch tape was applied to the back surface to act as a diffuser scattering the reflected light away from the detector. This tape technique was also used to isolate the film on the top surface where the incident beam overlapped the bare substrate and the film. A more complete discussion of the usage of tape is given in Appendix A. First, measurements of a bare GaAs substrate were taken and modelled using

WVASE to determine the native oxide present on the surface. ‘Built-in’ tabulated  $n$  and  $k$  values from unpublished data by the University of Nebraska, Lincoln were used for the GaAs substrate dielectric function. Dispersion relation parameters from Zollner [39] were used to model the native surface oxide. Once the oxide thickness was determined and the model for the substrate confirmed, a model describing the films was developed. This model consists of the GaAs substrate, the native oxide layer, a general oscillator layer representing the ZnO (typically aluminum doped ZnO produced by PLD was studied), and a top surface roughness layer using an effective medium approximation (EMA) of 50% ZnO and 50% void material. The general oscillator model for the aluminum doped ZnO films included a Tauc-Lorentz oscillator and a Drude oscillator. The Tauc-Lorentz oscillator models the behavior of amorphous materials well, particularly near the band gap [38]. Because the films in this study have a large free carrier concentration, a Drude oscillator is included in the model to capture the phenomenon of free carrier absorption at longer wavelengths approaching the plasma frequency. The functional form of the complex dielectric function,  $\epsilon_{T-L} = \epsilon_1 + i\epsilon_2$ , for the Tauc-Lorentz oscillator as a function of energy,  $E$ , is given by [38]

$$\begin{aligned} \epsilon_2 &= \begin{cases} \left[ \frac{AE_0C(E - E_g)}{(E^2 - E_0^2)^2 + C^2E^2} \frac{1}{E} \right] & E > E_g \\ \epsilon_2 = 0 & E \leq E_g \end{cases} \\ \text{and } \epsilon_1 &= \frac{2}{\pi} P \int_{E_g}^{\infty} \frac{\xi \epsilon_2(\xi)}{\xi^2 - E^2} d\xi. \end{aligned} \quad (2.10)$$

where  $A$  is the amplitude of the Tauc-Lorentz oscillator,  $E_0$  is the center energy,  $E_g$  is the band gap energy, and  $C$  is the oscillator broadening. The functional form of the ‘N-mu’ style Drude is given by Woollam [38] as

$$\epsilon_{Drude} = \frac{-\hbar^2}{\epsilon_0 \rho (\tau E^2 + i\hbar E)} \quad (2.11)$$

where  $\rho = \frac{m^*}{Nq^2\tau} = \frac{1}{q\mu N}$ ;  $N$  is the carrier concentration in  $\text{cm}^{-3}$ ,  $\mu$  is the mobility in  $\text{cm}^2(\text{V}\cdot\text{s})^{-1}$ ,  $m^*$  is the effective mass,  $\tau$  is the scattering time in s, and  $\hbar$  is the modified

Planck's constant.

The quality of the model's fit to the data, the mean square error (MSE), was calculated using the experimental standard deviation method and had typical values ranging from 4 to 15 as determined by [38]

$$MSE = \sqrt{\frac{1}{2N - M} \sum_{i=1}^N \left[ \left( \frac{\psi_i^{mod} - \psi_i^{exp}}{\sigma_{\psi,i}^{exp}} \right)^2 + \left( \frac{\Delta_i^{mod} - \Delta_i^{exp}}{\sigma_{\Delta,i}^{exp}} \right)^2 \right]} \quad (2.12)$$

where  $N$  is the number of data points ( $\psi$  and  $\delta$  at each wavelength),  $M$  is the number of fit parameters, and  $\sigma$  is the experimental standard deviation. Once a reasonable fit was achieved by adjusting the specified fitting parameters using the Levenberg-Marquardt multivariate regression algorithm to minimize the MSE, the optical constants could be used to determine the transmittance of the films. The extinction coefficient  $k$ , determined by the relations  $\epsilon_1 = n^2 - k^2$  and  $\epsilon_2 = 2nk$ , is used to calculate the absorption coefficient  $\alpha$  by [10]

$$\alpha = \frac{4\pi k}{\lambda} \quad (2.13)$$

Using Beer's Law we can write the transmission as [29]

$$T = \frac{I}{I_0} = \exp^{-\alpha t} \quad (2.14)$$

where  $I_0$  is the incident light intensity,  $I$  is the transmitted intensity, and  $t$  is the film thickness.

### 2.3.3 Other Routine Measurements

In addition to the measurements discussed in the proceeding sections, the following routine measurements using the devices listed were performed on the samples in the study.

- AFM - Veeco Multimode AFM
- Profilometry - Veeco Dektak 150
- XRD - Bruker D8 Discover
- UV-VIS-NIR Spectrophotometry - Cary 5G Spectrophotometer

- SEM - Hitachi S-5500 S(T)EM

CHAPTER 3  
RESULTS AND DISCUSSION

In this chapter I present the results of the experiments described and discuss the trends observed. For the sol-gel method the parameters varied were annealing temperature and annealing ambient. For the PLD films the variables adjusted were the growth temperature, annealing temperature, growth ambient, and annealing ambient. All films were nominally 100 nm thick.

### 3.1 Sol-gel – PLD Comparison

By incorporating Al doping and annealing in a reducing atmosphere, seemingly non-conductive ZnO thin films grown by the sol-gel method could be made conductive, however they lacked the quality achieved by even the as-deposited Al-doped PLD grown films. The resistivity of the films grown by the sol-gel process was on average 3 orders of magnitude larger than the PLD-grown films as shown in Table 3.1.

Table 3.1: Tabulated data comparing the resistivity, mobility, and carrier concentration between films grown using a sol-gel process and films deposited by PLD as a function of annealing temperature in forming gas atmosphere.

Films using sol-gel growth			
Anneal Temp (C)	Resistivity ( $\Omega\cdot\text{cm}$ )	Mobility ( $\text{cm}^2(\text{V}\cdot\text{s})^{-1}$ )	Carrier Conc. ( $\times 10^{20} \text{ cm}^{-3}$ )
470	150.	0.198	0.0210
530	33.4	0.0910	0.206
Films grown by PLD			
unannealed	0.267	0.772	3.24
470	0.0779	1.53	5.25
500	0.00949	3.17	2.08
530	0.0863	0.985	7.34

While the films grown from the sol-gel process show great improvement with the H anneal, they still lack the low resistivity necessary for application as a state-of-the-art TCO (Minami [4] states that a resistivity below  $10^{-3} \Omega\cdot\text{cm}$  and transparency  $>80\%$  are practical). The PLD grown films on the other hand, show a minimum resistivity of around  $9.5 \times 10^{-3} \Omega\cdot\text{cm}$  which is beginning to approach the level of quality TCOs. The increase in conductivity for these films has been explained by others [16, 22, 23] as H adsorption on the grain boundaries which serves to lower the potential barrier that charge carriers experience and allow the carriers to ‘hop’ from grain to grain thus increasing the mobility. Hydrogen also acts as a shallow donor in ZnO by ionizing to the  $\text{H}^+$  charge state, which is the only stable charge state in ZnO [40]. H can also indiffuse easily into ZnO and tends to fill oxygen vacancies thereby becoming a shallow donor [40]. The two doping mechanisms described above can be summarized as either interstitial or substitutional. The process by which H improves the conductivity of ZnO films in this study is most likely due to a combination of these effects which is dependant upon the relative defect densities [41].

For the films grown by the sol-gel method, the H is more likely to occupy interstitial sites because of trapping at defects [41]. Based on the electron mobility values of these films, it is reasonable to say there is a higher defect density in the sol-gel prepared films than the PLD ones. The sol-gel prepared films are quite often not stoichiometric (as is evident by their seemingly intrinsic n-type conductivity) and have a high density of oxygen vacancies which the H can occupy as a substitutional  $\text{H}^+$  impurity. Therefore, both of these doping mechanisms can potentially be the source of the increased conductivity after the H anneal. The PLD grown films, on the other hand, show a higher electron mobility indicating less defect scattering making it more likely that the improved conductivity comes from the substitutional incorporation of H. Because these films have less defect density than the sol-gel deposited films there is a greater chance that H occupies a substitutional position on the oxygen site, which according to the DFT calculations by van de Walle [40] is energetically favorable. However, there is still much debate over the effects of H as a

dopant in semiconductors especially concerning the two areas of whether or not it is the dominate dopant in certain circumstances [41] and also the mechanism by which it dopes the films. Furthermore, King and Veal [41] make note that using different growth techniques can produce films with different sources of conductivity (e.g. impurity doping like Al or native defect doping like Zn interstitials or oxygen vacancies) and because of these differences in doping mechanisms, the effects of H are not universal beyond the specific material being studied. It has been shown in this study that heat treating both PLD grown films and films deposited via the sol-gel method in hydrogen gas after deposition generally increases the conductivity of the films *caeteris paribus*. However, the increase in conductivity is not as great for the PLD grown films perhaps due to the better structural quality of the films made by PLD (indicated by a higher electron mobility) thus reducing hydrogen incorporation into defect sites. An SEM cross-section of a typical PLD film showing the micro-structure of the ZnO film is presented in Figure 3.1.

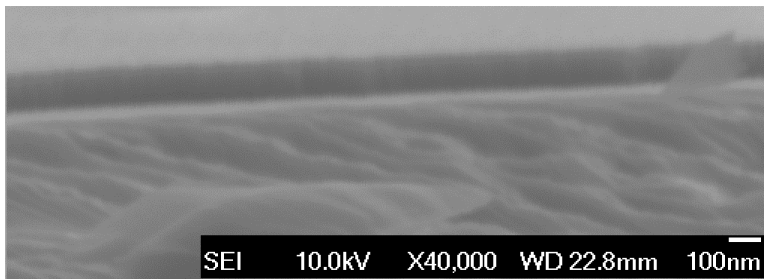


Figure 3.1: SEM cross-section of a typical ZnO film on GaAs substrate with a thickness of approximately 124 nm showing the high quality film grown by PLD.

### 3.2 Growth on GaAs Substrates

The experiments exploring the growth on GaAs can be grouped into three different categories depending on the parameter being investigated: ambient gas composition, growth temperature, and post-deposition treatments. These three categories are discussed in the following subsections.

### 3.2.1 Ambient Gas Series

The resistivity, carrier concentration, and mobility of the films as a function of ambient growth pressure are shown in Figure 3.2. For room temperature growth in oxygen, the resistivity has a minimum value of  $5.7 \times 10^{-4} \Omega \cdot \text{cm}$  at a pressure of 0.01 mbar. At this pressure, the Knudsen number,  $0.01 < Kn < 1$  puts the process in an intermediate regime between the high-vacuum and fluid-flow processes such that the species interacting with the oxygen background gas sufficiently incorporates enough oxygen to minimize defect scattering from oxygen vacancies while still having the required surface mobility to find ledge and kink sites to increase the film quality and thus increase the Hall mobility, a trend that is shown in Figure 3.2c where the mobility (and to a limited extent the carrier concentration) peaks at 0.01 mbar leading to the lowest resistivity occurring at this pressure.

On a side note, the terminology used to describe crystalline materials is often used for amorphous (or even organic) materials as well. Cho, Kim, and Hwang [42] make the argument that amorphous ZnO and crystalline ZnO should share similar electronic properties despite the difference in crystal structure. One point they bring up is that there are no distinct grain boundaries in completely amorphous films and single crystals to disrupt electron transport like in polycrystalline ZnO. While the physics fundamentally differ between amorphous and crystalline materials, the apparent effects are described very well in terms of crystalline systems and as such some of the associated terminology will be used herein.

An increase in scattering (or reduction in the mobility from the reduction in structural quality) is credited with inhibiting the conductivity of these films. Often, the dominate scattering mechanism is attributed to ionized impurity scattering when the carrier concentration is  $> 10^{19} \text{ cm}^{-3}$  [26, 43] but Ellmer and Mientus report that grain barrier traps can play a significant role in AZO films in limiting the mobility up to  $n \approx 10^{20} \text{ cm}^{-3}$  [44, 45]. The term ‘grain’ is used loosely and is generally referring to a boundary between structural areas where the packing of molecules could change or where bond angles are particularly strained. These boundaries could arise from the coalescing of islands during growth as in the

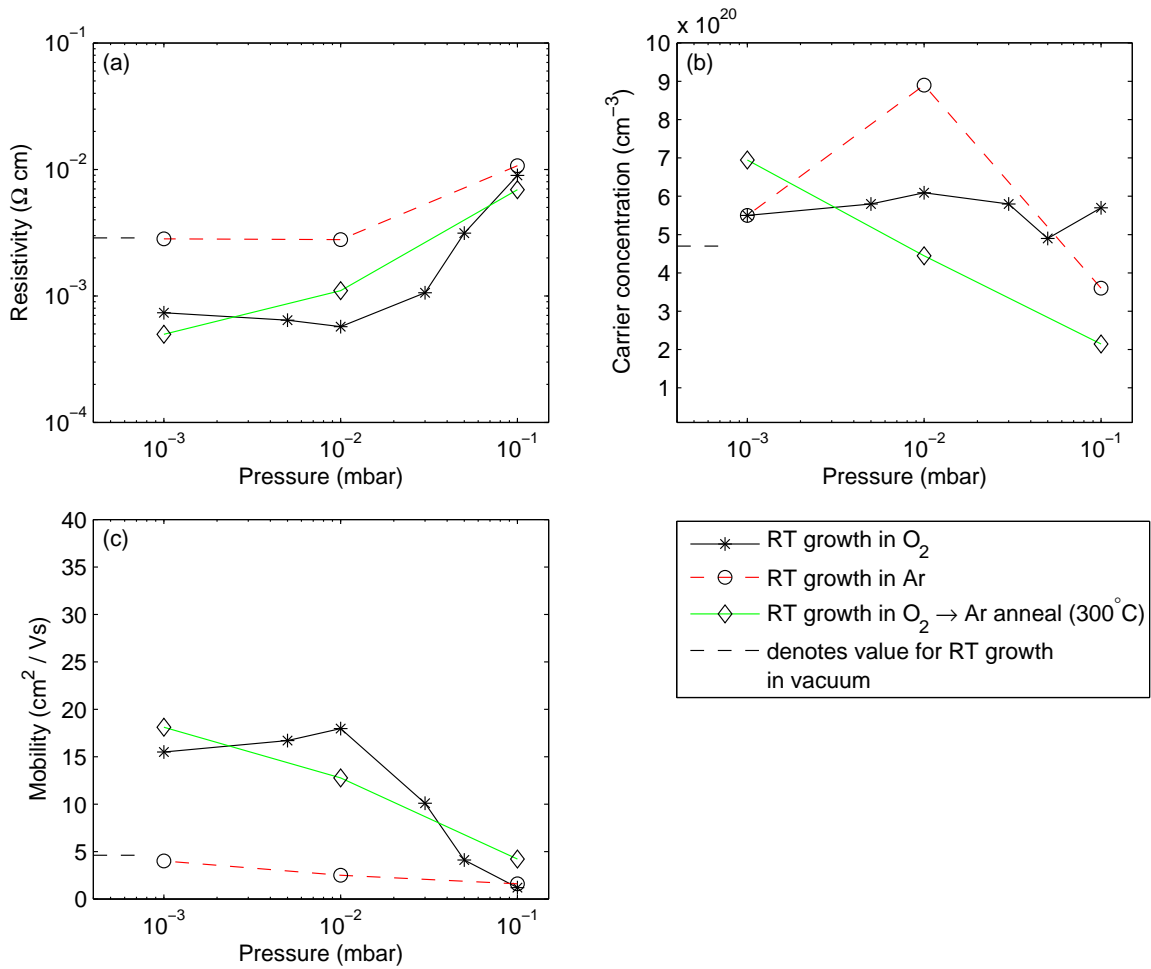


Figure 3.2: Resistivity (a) carrier concentration (b) and mobility (c) for the AZO films grown on GaAs substrates as a function of ambient pressure during growth. The post-anneal (shown for comparison) was performed at a pressure of 0.5 mbar for 2 hr.

Volmer-Weber model. The carrier concentrations of the films in this series are on the same order of magnitude as in the study by Ellmer making this scattering mechanism applicable. With these films being amorphous to slightly nanocrystalline, lattice scattering is another mechanism that is potentially present on short length scales where the ‘short-ness’ is in comparison to the size of the grains present. XRD measurements taken on these samples show a very small peak for the lowest resistivity film at  $\sim 34^\circ$  corresponding to the (0002) plane. However, for the majority of the samples grown at RT no such peak was observed, but this doesn’t rule out the possibility of short-range order (i.e. nanocrystallinity). For example, Gondoni *et al.* [28] report ZnO(0002) crystal structure for films grown at RT which they were able to measure with thicker samples ( $>500$  nm) on Si substrates, therefore the potential exists that the films in this work could have nanocrystalline features as well that the XRD measurements performed herein were not particularly sensitive to. With lattice scattering, disruptions in the periodic potential of the lattice (often resulting from thermal vibrations, i.e. phonons) cause the charge carriers to be deflected and thus lower the mobility [29]. However, because these films are generally amorphous the ‘lattice’ vibrations in this sense are short-range localized disruptions of individual atoms or molecules about their equilibrium positions that serve to scatter the charge carriers as opposed to longer range vibrations of the entire lattice (true phonon scattering). Furthermore, the defects in the ‘lattice’ referred to above are likewise localized defects like oxygen vacancies, zinc interstitials, unterminated bonds, or strain in the bonds of the material where the local order is disturbed.

Assuming these scattering mechanisms are independent of each other, the probability of scattering from each mechanism can simply be summed [29]

$$\frac{dt}{\tau} = \frac{dt}{\tau_I} + \frac{dt}{\tau_L} + \frac{dt}{\tau_D} \quad (3.1)$$

where  $dt$  is the differential time that the scattering event occurs in divided by the mean time between collisions  $\tau$  for each scattering type discussed below. Relating the mobility to the scattering time as  $\mu = \frac{e\tau}{m^*}$  we can write the total mobility as  $\frac{1}{\mu} = \frac{1}{\mu_I} + \frac{1}{\mu_L} + \frac{1}{\mu_D}$  where  $\mu_I$  is the mobility considering only ionized impurity scattering,  $\mu_L$  is the mobility if only

lattice scattering were present, and  $\mu_D$  is the scattering caused by defects not included in the other two mobilities [29]. We can then observe that the total mobility is smaller than any of the individual mobilities. If one of these mobilities is small compared to the others, it will effectively pin the mobility at this lower value so in order to improve the net mobility all of the scattering mechanisms need improvement to avoid one scattering mechanism throttling the mobility.

Further evidence supporting this conclusion is given by the films grown in Ar background gas; the mobility steadily decreases as the pressure increases as shown in Figure 3.2c, indicating that deflecting off the ambient gas molecules lowers the energy available for surface diffusion (i.e. effective  $kT$  energy used in Eq. 2.3) of the impinging species thus causing an increase in defect scattering as the adatoms are not reorganizing to their lowest energy configuration. This deficiency in surface mobility of growth species manifests itself in the root-mean-square (RMS) surface roughness as measured by AFM (for films grown at various oxygen pressures). As the pressure increases the surface roughness increases rapidly as shown in Figure 3.3. The increase in surface roughness indicates that the surface mobility of the adatoms is reduced because they fail to move to terrace edges creating a smoother surface like the films grown at lower pressures. It could be argued that the growth rate might impact the roughness by creating rougher surfaces for faster rates as the adatoms would not have time to reorganize before another layer is deposited but the growth rate was actually slower for higher pressures thus ruling that possibility out. It is therefore rather conclusive that increasing the ambient pressure causes a reduction in the quality of the film's structure. Martinez *et al.* [46] have shown a similar degradation for films grown by rf sputtering. Because the XRD data sheds no light on the crystallographic quality of these films we must rely on AFM measurements to draw these conclusions. It is also interesting to note that Igasaki and Saito [47] notice very similar trends in their films grown on sapphire albeit over a smaller temperature of 50 C to 400 C.

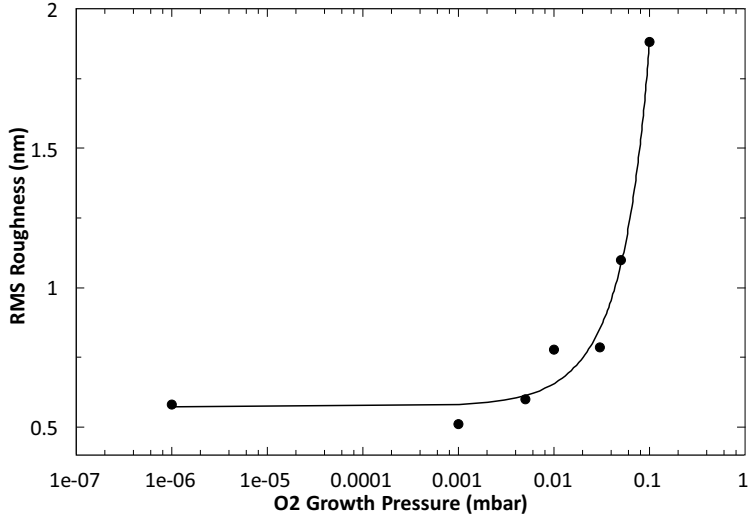


Figure 3.3: Root-mean-square surface roughness as a function of ambient oxygen pressure during growth as determined by AFM.

To summarize, the defects in the lattice caused by oxygen vacancies at low pressures or defects induced by limited surface diffusion at high pressures help to explain why the Hall mobility decreases for all the samples grown at higher pressures and why the mobility decreases at low pressures for the growth in oxygen shown in Figure 3.2.

The electrical resistivity is low enough to suitably satisfy the ‘C’ part of TCO (State-of-the-art ITO reported in 2010 by Tuna *et al.* [48] have a resistivity of  $1.5 \times 10^{-4} \Omega\cdot\text{cm}$ ) just leaving the transparency to be confirmed. After modelling the ellipsometry data for these films, plotting the transmission  $T(\%)$  as a function of  $\lambda$  as described in Equation 2.14 gives the transmittance spectra shown in Figure 3.4. Note that the transmission in this case is calculated from the absorption coefficient and is thus higher than the transmission measured by spectrophotometry because the calculation herein does not take into account reflection at the interfaces. A schematic representation of the model for these films is shown in Figure 3.5 and discussed in Section 2.3.2. The highest conductivity films in the pressure series shown in Figure 3.4 are >90% transparent in the visible region indicating that these films are acceptable TCOs [28, 48, 49]. The ITO films from Tuna [48] are  $\sim 85\%$  transparent in the

visible region. Near the optical gap, the films grown at low ambient pressures show decreased transmission and not as sharp of a transition between absorbing and transmitting. As the growth pressure increases, the transmission near the optical gap edge also increases. This trend can be explained by considering the stoichiometry of the films. As oxygen pressure decreases, more oxygen vacancies develop which can lead to sub-band gap transitions in the films and thus absorbency below the band gap energy [50]. In the region from 500 nm to 700 nm, all films except the in-vacuum growth show very similar transmission. At longer wavelengths, the transmission at particular wavelengths again shows a dependence on growth pressure. As the growth pressure increases, the transparency increases and peaks with the 0.03 mbar before decreasing again analogous to the trend seen in the resistivity data. Furthermore, at these longer wavelengths the tail of a broad free carrier absorption peak is present but is not very strong in this region because it is above the plasma frequency calculated by [10]

$$\omega_p = \sqrt{\frac{ne^2}{\epsilon_\infty \epsilon_0 m^*}} \quad (3.2)$$

where  $N$  is the carrier concentration,  $e$  is the electric charge,  $\epsilon_\infty$  is the dielectric constant at zero energy (infinite wavelength),  $\epsilon_0$  is the permittivity of free space, and  $m^*$  is the effective mass. For the lowest resistivity sample the plasma frequency is calculated as  $1.79 \times 10^{14}$  Hz or 1670 nm in wavelength using  $n = 6.1 \times 10^{20} \text{ cm}^{-3}$  from Hall effect measurements,  $\epsilon_\infty = 4$  [11], and  $m^* = 0.38m_e$  (averaged from [11, 51]). This value for  $\omega_p$  puts the plasma absorption in the IR resulting in a transparent ‘window’ from the optical gap near the plasma absorption edge as roughly  $1670 \text{ nm} - 370 \text{ nm} = 1300 \text{ nm}$  wide. The spectroscopic ellipsometry data for the optimal film has a range of 360 nm to 1300 nm but extrapolating the model further yields the transmission spectrum shown in Figure 3.6. In addition to the absorption coefficient the calculated values for the index of refraction,  $n$ , and the extinction coefficient,  $k$ , are also important in determining the optical properties of the films and are shown in Figure 3.8 for the optimal film. All other films have the same general shape for  $n$  and  $k$  but the magnitude

of  $k$  tends to vary and leads to the differences in transmission shown here.

In order to further verify that the ellipsometry modelling is correct, films were grown on glass under the optimal conditions of RT and 0.01 mbar O<sub>2</sub>. While the purpose of this thesis is to explore the effects of growing on GaAs substrates, growing films on glass allows me to corroborate the calculated transmission with spectrophotometric measurements. For the UV-Vis-NIR Spectrophotometric measurements, a zero/baseline correction was used. The 100% transmission baseline was taken not going through a blank piece of glass but rather just the standard sample holder so that when the actual transmission measurement was taken, the glass was not ‘subtracted out.’ This was done in order to compare the measurement to the transmission calculation done in WVASE by the transfer matrix method which also did not ‘subtract out’ the glass. Note that this transmission is not the same as the transmission calculated by Eq 2.14 because it takes into account the reflection and absorption components as well. Results are shown in Figure 3.7. While the interference oscillations do not match up exactly for these two techniques, the average over the visible spectrum ( $\sim 370$  nm - 750 nm) is quite consistent leading to the conclusion that the model accurately describes reality.

A comparison of the optimized film grown at 0.01 mbar in this study to other similar films reported in the literature reveals good agreement for growth on different substrates with similar process parameters as shown in Table 3.2 thus confirming GaAs substrates can support quality room temperature (RT) deposited AZO layers as TCOs. The optimized ambient gas composition and pressure from this series were next used to explore the effects of the other parameters (substrate temperature and annealing affects).

### 3.2.2 Growth Temperature Series

In this series of depositions the temperature of the GaAs substrate was varied in 100 degree increments from RT to 500 C with an ambient oxygen pressure of 0.01 mbar. Hall measurements on these samples show that the resistivity is fairly constant from RT to 200 C before increasing to a maximum of  $4.3 \times 10^{-3} \Omega\text{-cm}$  at 400 C as shown in Figure 3.9. It can be seen that both the mobility and the carrier concentration fall sharply at 300 C and 400 C

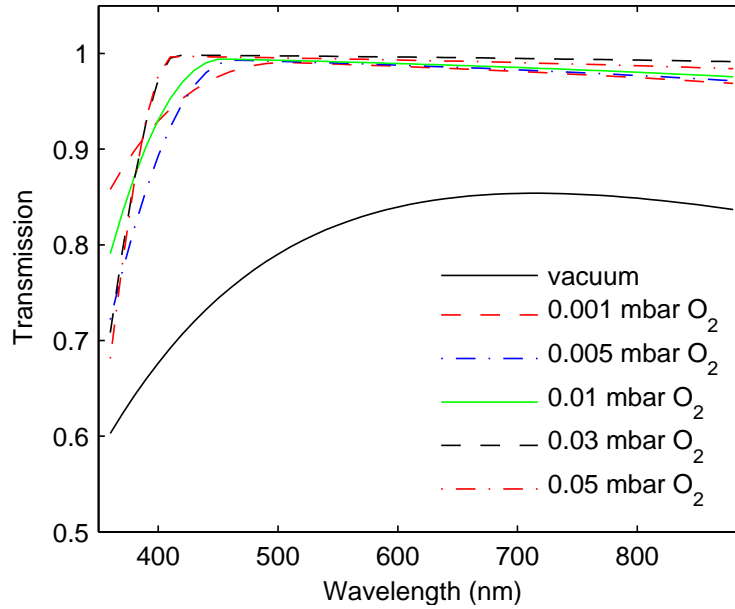


Figure 3.4: Calculated transmission from  $T = \exp(-\alpha t)$  for AZO films grown at RT in the oxygen pressure indicated.

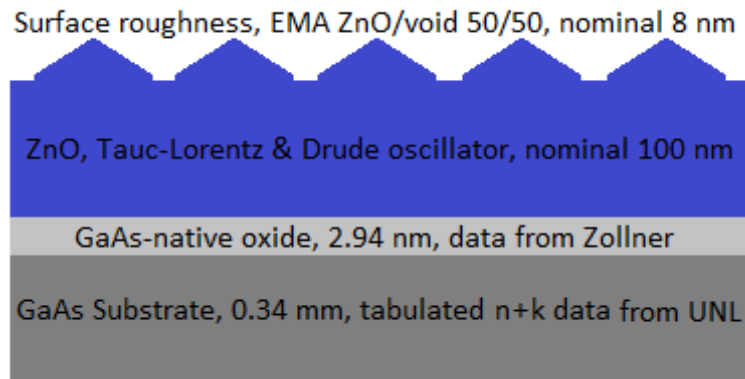


Figure 3.5: Schematic representation of the layers used to model the ellipsometric data.

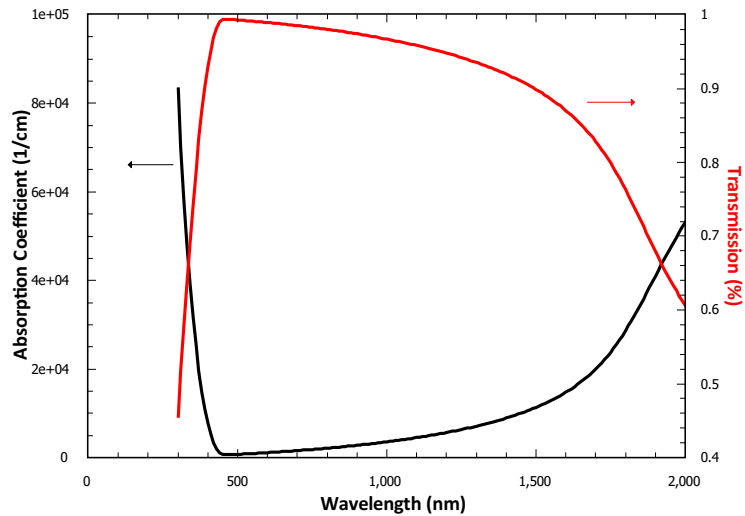


Figure 3.6: Transmission calculated from absorption coefficient and extrapolating the model for the optimal film.

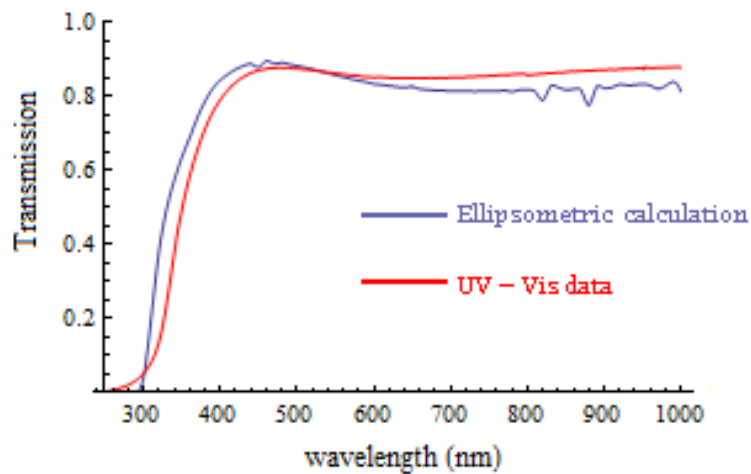


Figure 3.7: Transmission through film and glass substrate from UV-Vis-NIR spectrophotometry measurements and calculated transmission from  $n$  and  $k$  values determined with ellipsometry.

Table 3.2: Resistivity values for RT growth compared to literature reports also at RT including the process pressure, substrate, and transparency.

Resistivity ( $\Omega\cdot\text{cm}$ )	O <sub>2</sub> Pressure (mbar)	Substrate	%T	Ref.
$5.7 \times 10^{-4}$	0.01	GaAs	$\sim 90-95^*$	This work
$4.5 \times 10^{-4}$	0.02	Si & glass	$\sim 80$	[28]
$7.33 \times 10^{-4}$	0.0013	glass	86	[11]
$6.11 \times 10^{-4}$ (opt. meas.)	0.01	glass	$\sim 85$	[52]

\*calculated transmission from absorption coefficient

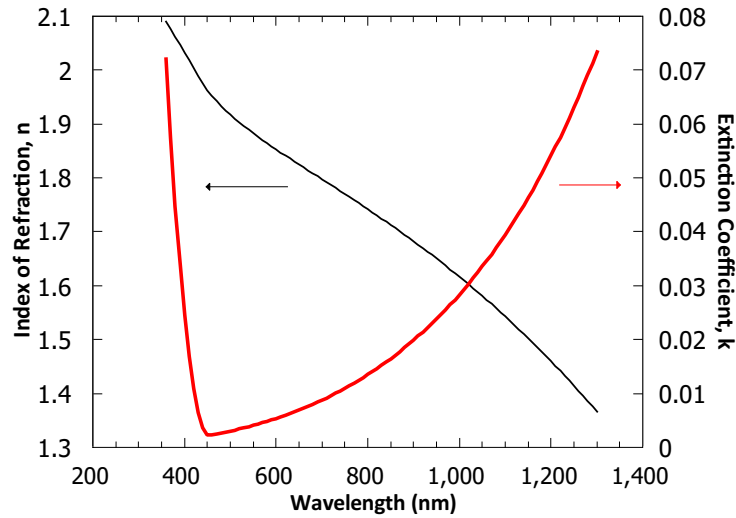


Figure 3.8: Calculated  $n$  and  $k$  values for lowest resistivity sample grown at RT in 0.01 mbar O<sub>2</sub> by PLD on GaAs. Note the sharp increase in  $k$  as the wavelength decreases showing the onset of band-to-band transitions and thus increased absorption in the films.

growth temperatures indicating possible dopant deactivation as discussed before. Figure 3.10 shows XRD measurements performed on these samples. The peak corresponds to the (0002) crystallographic structure. As the temperature increases there is a peak shift indicating strain in the system that could be caused by the non-epitaxial growth. The lattice constant,  $c$ , the full-width at half-max (FWHM), and the peak position are shown in Table Table 3.3. From the XRD data, grain size can be calculated using the Scherrer formula [53]

$$\frac{0.9\lambda}{\cos(\theta)\sqrt{\beta^2 - \beta_i^2}} \quad (3.3)$$

with  $\beta_i$  and  $\beta$  being the broadening correction factor due to the instrumental setup and the FWHM determined from the XRD measurements, respectively. The samples display monotonically increasing crystallinity with increasing growth temperature implying that the mobility should also be improving as well because scattering off grain boundaries should be decreasing as the grains get larger. The calculated grain sizes are plotted in Figure 3.11.

Table 3.3: Summary of the FWHM, lattice constant, and peak position determined from XRD measurements.

Growth Temp.	100 C	200 C	300 C	400 C	500 C
FWHM ( $^\circ$ )	0.47	0.44	0.34	0.35	0.29
Lattice Constant, $c$ ( $\text{\AA}$ )	5.2414	5.2235	5.2024	5.1876	5.1834
Peak Position ( $^\circ$ )	34.186	34.307	34.451	34.552	34.581

However, seeing the large dip in mobility at 300 C and 400 C indicates an increase in scattering seemingly not associated with lattice scattering (i.e. better crystallinity). It has been reported in the literature that  $\text{Al}_2\text{O}_3$  compounds like  $\text{Al}_2\text{O}_3(\text{ZnO})_3$  and  $\text{ZnAl}_2\text{O}_4$  can form in these films [26, 54–56]. I speculate that the formation of these compounds would lead to increased impurity scattering thus lowering the mobility. Also, Al atoms would be used to create these compounds lowering the availability of Al to dope the films, thereby reducing the carrier concentration, which is consistent with the Hall effect measurements and the results reported in the literature cited above. The increase in crystallinity but

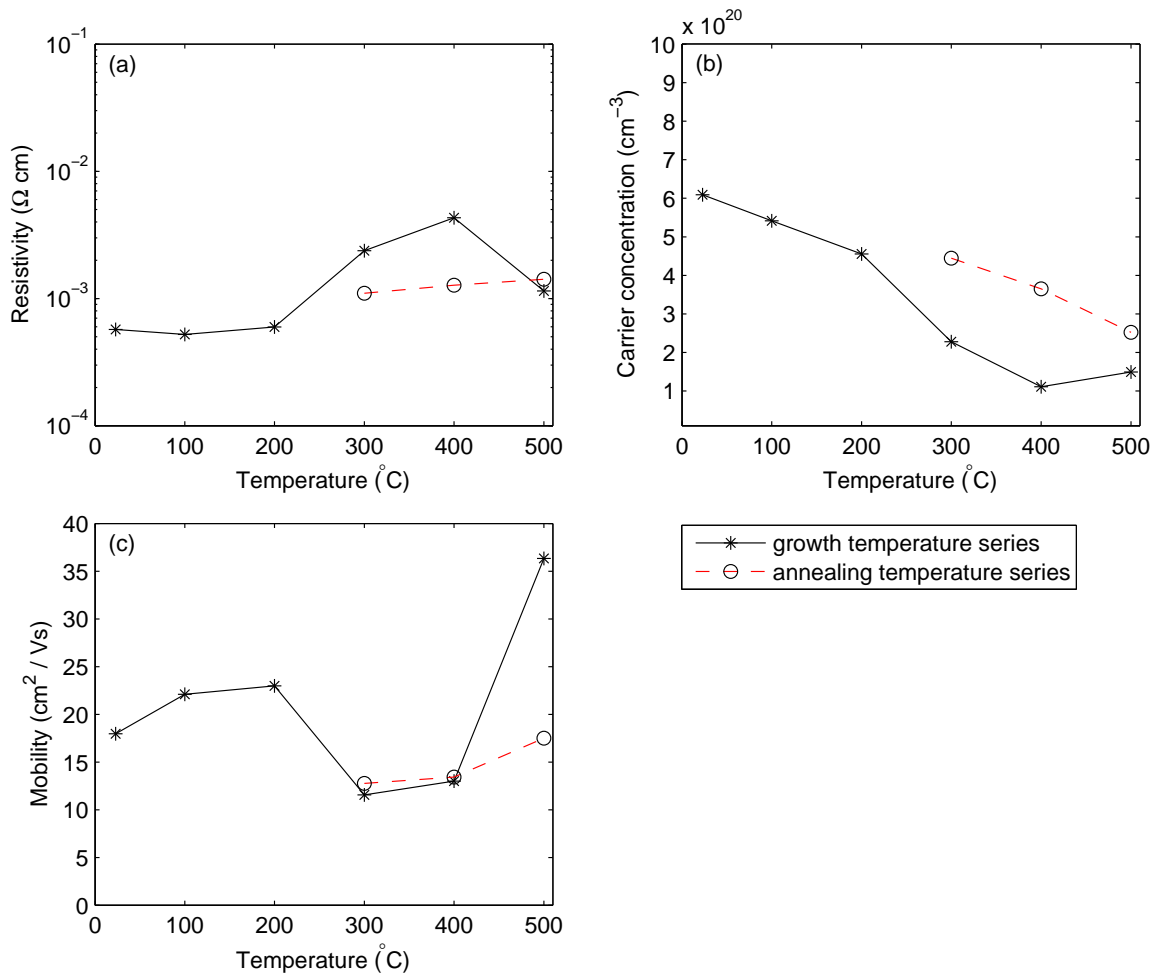


Figure 3.9: Resistivity (a), carrier concentration (b) and Hall mobility (c) as a function of temperature. All films were grown in a 0.01 mbar oxygen ambient. Post-deposition annealing occurred for two hours in 0.5 mbar Ar on samples grown at RT, with 0.01 mbar oxygen (shown for comparison).

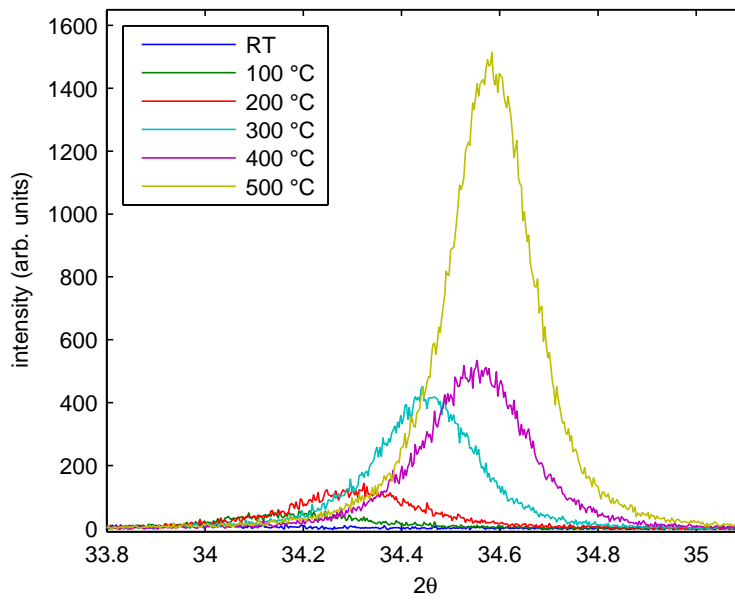


Figure 3.10: XRD  $2\theta$  measurements as a function of growth temperature.

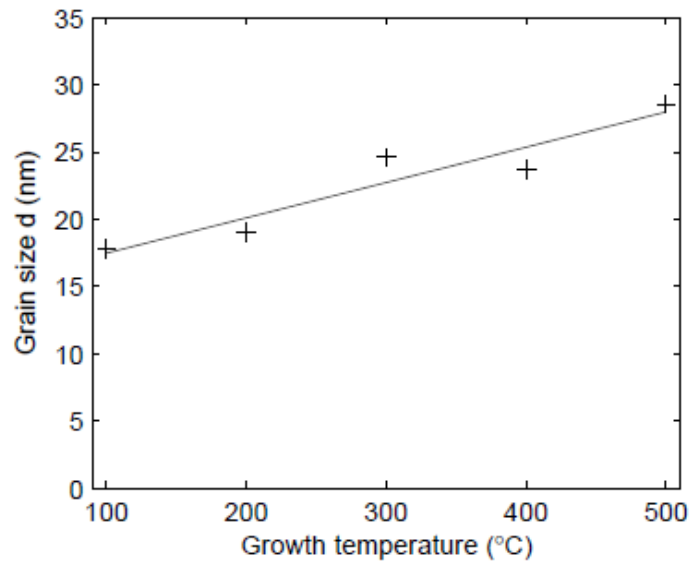


Figure 3.11: Grain size as a function of growth temperature calculated from the Scherrer formula for films grown in 0.01 mbar oxygen ambient.

decrease in mobility is not consistent implying defect formation is increasing in these films. Another interesting point along these lines is that the surface roughness of these films were all nominally the same and showed no trend or variation with growth temperature, perhaps indicating competing mechanisms affecting surface roughness.

Despite increased crystallinity, the conductivity of these films grown at higher temperature does not exceed that of the RT growth. When using this growth process to make an actual device, increased temperature can cause problems with overall device quality. As the temperature increases, the ability of atoms to diffuse throughout the sample increases and can lead to poorer devices. Take a p-n junction, for example, the dopants used to create the p-n junction can diffuse within the sample if temperatures become elevated. This inter-diffusion would tend to smear out the p-n junction and reduce device performance. In the case of growing a TCO on such a device, it is beneficial to keep the sample at lower temperatures to prevent this unwanted diffusion, therefore not only are these films more conductive with RT growth, it is a great benefit to device processing to be able to grow at such low temperatures. Hunsperger [57] *et al.* saw diffusion of Be at temperatures as low as 600 C. With the p-n junctions present in these nanorod devices being on such a small scale, any diffusion could potentially ruin a device. One last benefit of low-temp processing is the energy savings (and time savings as well) from not having to heat samples. Reducing cost and time of processing is important in the competitive semiconductor industry.

The transparency of the films grown at various temperatures calculated from ellipsometry results is shown in Figure 3.12. The transparency is all-around higher for films grown at a higher temperature. The better crystal quality for films grown at higher temperatures allows for increased transmission by reducing the number of defects that allow sub-band gap transitions.

### 3.2.3 Post-deposition Treatments

Samples grown at room temperature using PLD at the optimum pressure of 0.01 mbar on GaAs substrates were annealed in oxygen, argon, vacuum, and hydrogen ambient gases.

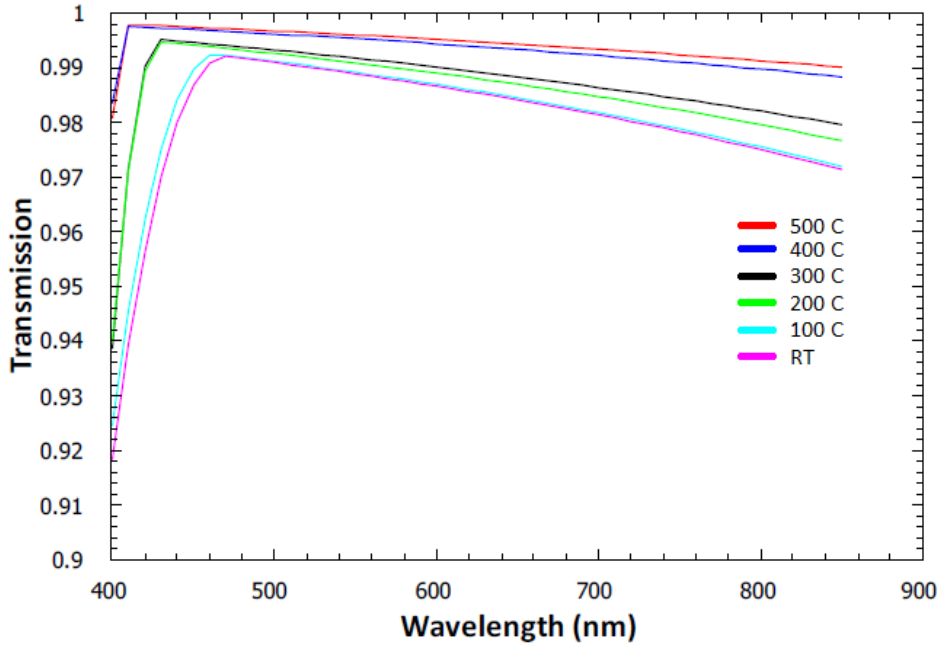


Figure 3.12: Calculated transmission spectra of films deposited at different growth temperatures on GaAs substrates at 0.01 mbar O<sub>2</sub> partial pressure.

A summary of the results for the anneals in oxygen, argon, and vacuum are shown in Figure 3.13. Annealing results at various temperatures and pressures are also shown in Figure 3.9 and Figure 3.2, respectively, in order to compare them to the as-deposited films. It is interesting to note that despite the widespread use of annealing to improve thin film properties, none of the anneals performed on the samples grown on GaAs by PLD showed improvement of any kind. XRD measurements show only a weak increase in crystallinity with no clear peak. Annealing in H also had a detrimental effect on the conductivity of these films. The resistivity increased from  $5.7 \times 10^{-4} \Omega\cdot\text{cm}$  to  $1.7 \times 10^{-3} \Omega\cdot\text{cm}$ . This change was mainly due to a drop in the mobility from around  $19 \text{ cm}^2(\text{V}\cdot\text{s})^{-1}$  to  $10 \text{ cm}^2(\text{V}\cdot\text{s})^{-1}$  when annealed at 500 C for 1 hr. The negative effects witnessed are attributed to dopant deactivation whereby dopants in the film, oxygen vacancies for example, are removed (deactivated) by the high temperature providing the necessary energy for that state to be filled or removed from the film. Like the growth at increased temperature, the annealing treatments produce poor electronic quality films and could negatively impact device processing so RT growth without

annealing was used to create some preliminary devices discussed in the next section.

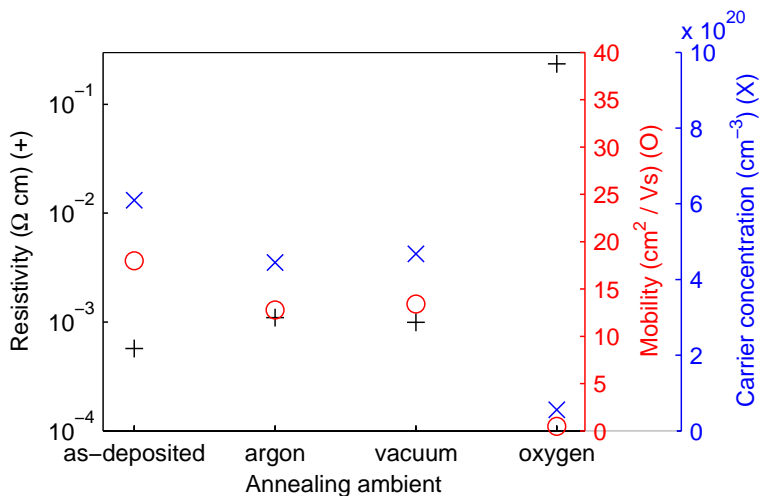


Figure 3.13: Resistivity, carrier concentration and Hall mobility as a function of ambient gas during post-deposition annealing at 300 C. The AZO films were deposited at RT in 0.01 mbar oxygen ambient gas.

### 3.3 Applications to Devices

The optimized growth conditions (0.01 mbar oxygen pressure at RT) for PLD films on GaAs substrates were used to grow a TCO top contact on GaAs nanorod photovoltaic devices. Two general device morphologies were explored: densely packed rods and sparse rods. Figure 3.14 and Figure 3.15 show the “pre-ZnO deposition” morphologies for sparse and dense rods, respectively. The rods grown by Dheeraj Dasa were on average 100 nm in diameter and 0.7  $\mu\text{m}$  to 2  $\mu\text{m}$  long. More information about the specific rod used can be found at [12].

These two samples are typical of the starting nanorod arrays before deposition. The ZnO was then deposited at 0.01 mbar O<sub>2</sub> pressure at RT. Interestingly, depositing for the same time as the planar samples led to coatings about half as thick. This could be because the increased surface area of the rods requires more material to grow a layer of the same thickness or perhaps this indicates some anisotropy where the growth on the planar surface is faster than growth on the surface of the rods, which will be called the ‘shell’ from here on.

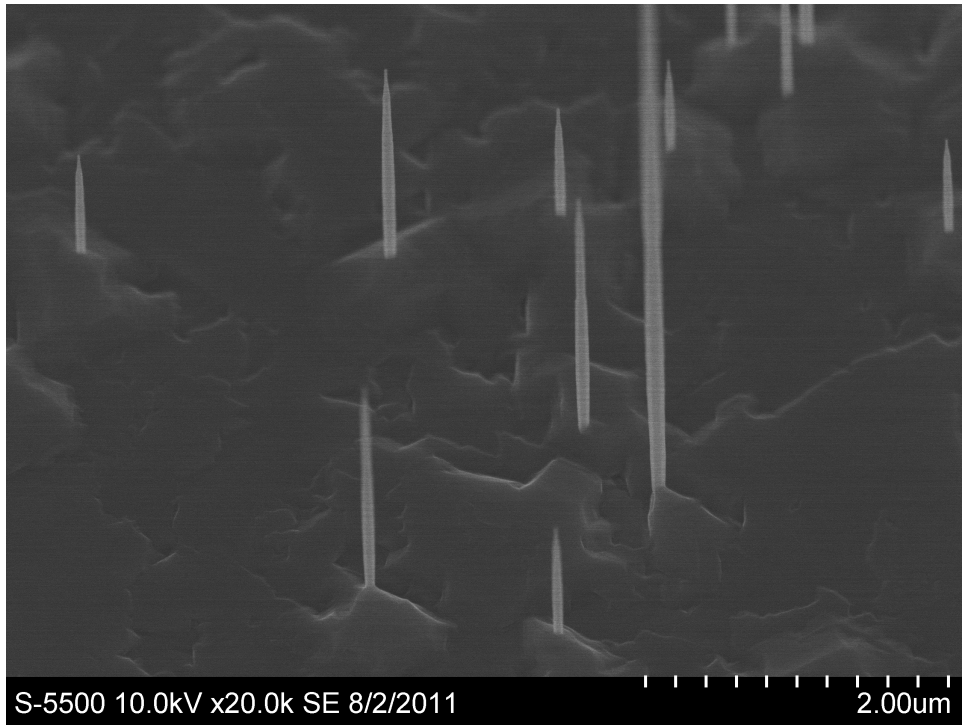


Figure 3.14: Sparsely packed GaAs nanorods before ZnO deposition.

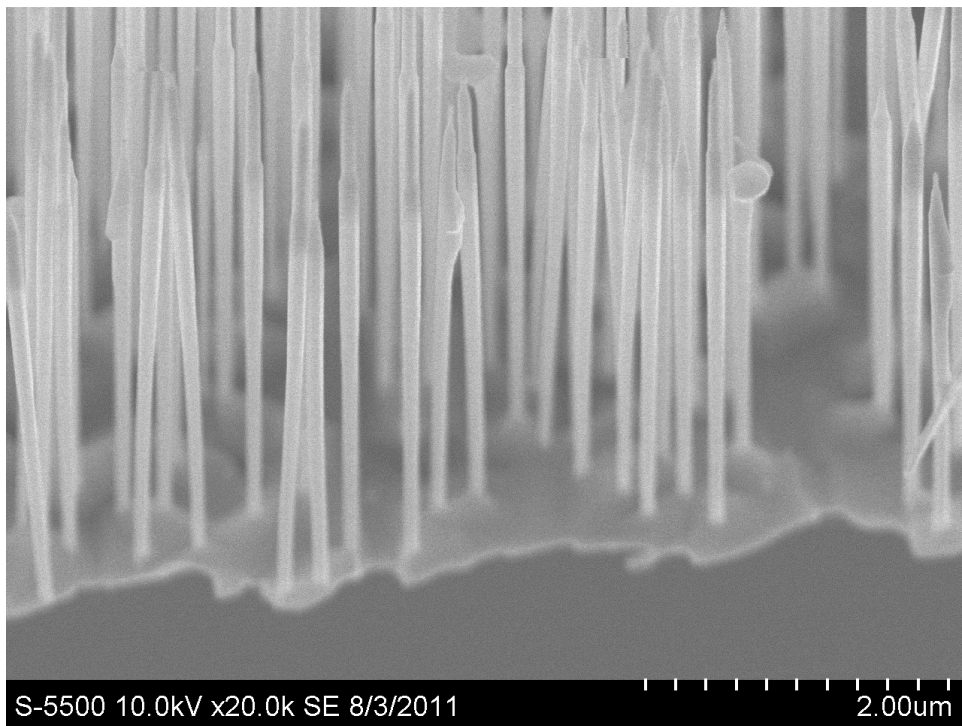


Figure 3.15: Densely packed GaAs nanorods before ZnO deposition.

The shell thickness was determined by measuring the diameter of the rods before and after deposition, subtracting the two, and dividing by 2. Post-deposition SEM images are shown in Figure 3.16 and Figure 3.17.

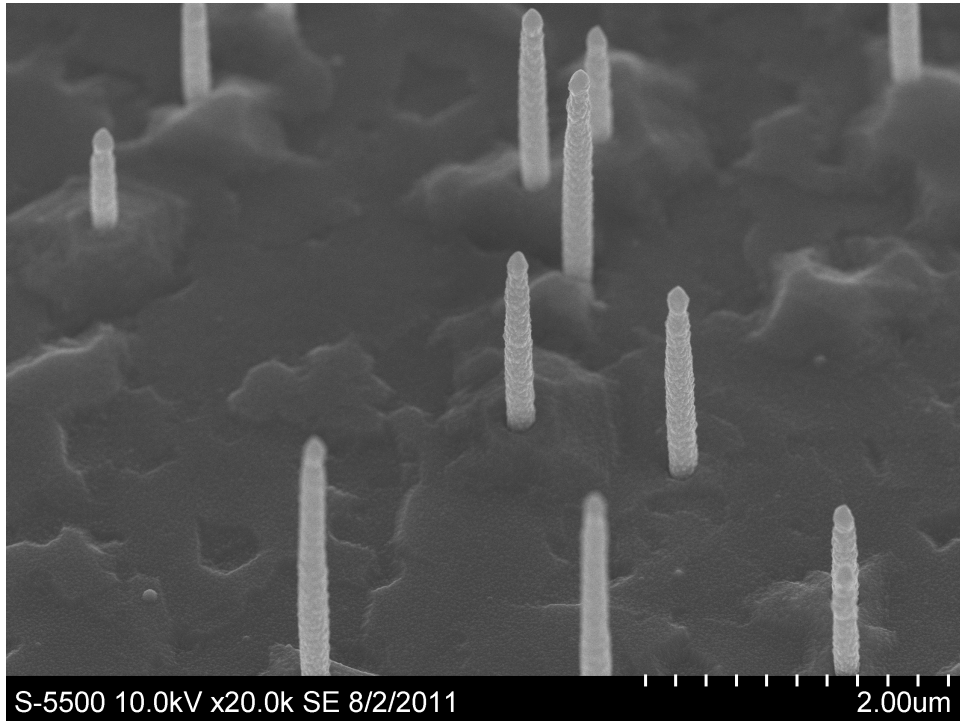


Figure 3.16: Sparsely packed GaAs nanorods after ZnO deposition.

Unfortunately, these devices were not functional solar cells due to flaws with the p-n junction (which is outside the scope of this work) in the GaAs rods for the sparse rods while for the dense rods shown in Figure 3.17 a p-n junction was not grown into the rods because they were intended to be a test to see if the PLD method could make conformal shells and a continuous base layer connecting all the rods. To determine the continuity of the base layer, I-V curves were taken across the surface of the dense rod sample. The curves were linear and from the slope of the line a resistance of only a few Ohms was calculated indicating a continuous conducting film was present between the rods. For the sparsely populated sample, an SEM image of the base of a rod shows some separation between the bottom of the rod and the base layer AZO film, which could pose problems with collecting current from

the rod in a working device but estimates of the shell thickness would suggest that the rod is fully in contact with the base layer (see Figure 3.18). This type of contact is necessary with the geometry of the sample because the traditional fingers and buses used for planar devices would not be able to penetrate between the dense rods and would cause shading to occur thus lowering the device efficiency.

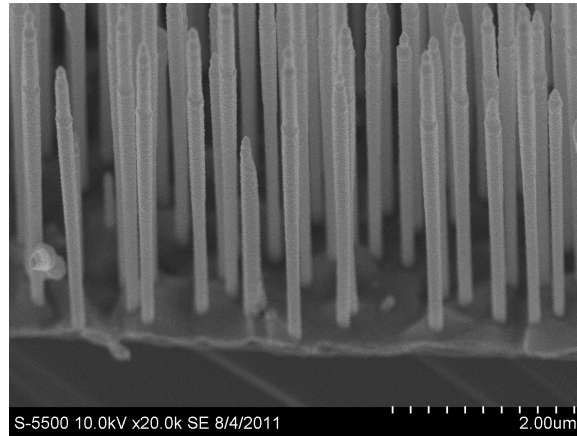


Figure 3.17: Densely packed GaAs nanorods after ZnO deposition.

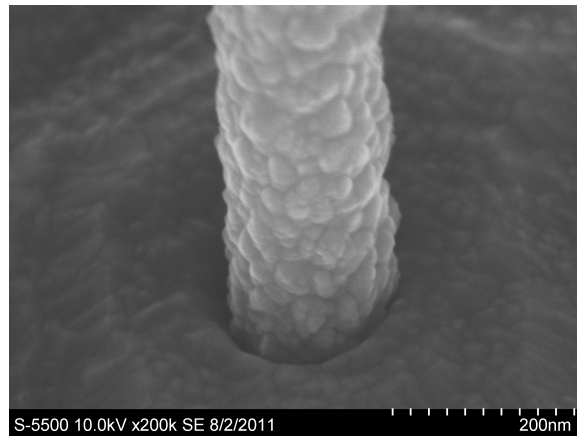


Figure 3.18: SEM image showing the region where the ZnO shell at the base of the rod interfaces with the ZnO film on the surface of the GaAs substrate. There appears to be contact implying current could be collected from the rod.

## CHAPTER 4

### CONCLUSIONS

In order to improve current solid state device technology, this thesis explored the effects of growth conditions and post-deposition heat treatments on the electrical resistivity and optical/visible transmission of ZnO. A recipe for minimizing the resistivity and maximizing the transparency using pulsed laser deposition is given for growth on GaAs substrates and nanostructures. The optimized film grown on GaAs meets the requirements for a transparent conducting oxide and actually out-performs the higher temperature growth, which was surprising at first but once all of the factors were analyzed the trends fit with the evidence of dopant deactivation, balancing oxygen pressure, and crystallinity effects. The two figures of merit (high conductivity and high transparency) rank the films grown herein among some of the best reported [5]. In order to make films extremely conducting, one could just naively increase the doping levels but two problems arise: one, the impurity scattering increases with increasing carrier concentration so the mobility decreases making the process counter-productive past a certain optimal point and two, as the number of free carriers increases, the window where the film is transparent shrinks as absorption from these free carriers becomes more pronounced. The goal of this work was to find an optimal balance between these competing effects while at the same time applying these films to devices without any ‘collateral’ damage (i.e. causing the p-n junction to lose its abruptness through diffusion). In regards to the morphology, the latter goal was achieved but inherent problems in the p-n junction of the nanorod solar cell precluded obtaining working devices. Future work by my colleagues in Norway will hopefully overcome this barrier and achieve functional devices. Future experiments would be to optimize and control the growth of the core and shell of the GaAs rods in order to not have the core exposed as was the case in several failed samples and also to precisely control the p-n junctions properties (i.e. doping concentration, depletion width,

impurities) so that working devices can be achieved.

As a simple process to follow, the work with sol-gel made it easier to develop annealing procedures and test measurement techniques. Had the work led to low resistivity and high transparency it would be a lower cost wet-solution process for making window layers on GaAs. While useful for developing measurement techniques and as a comparison to PLD, the results show that sol-gel preparation of Al-doped ZnO films is probably not suitable at the device level. The effects of hydrogen are still controversial. The results of this study shed no further light on the matter as mixed results were obtained where the films made by sol-gel responded very strongly to the H anneal but the PLD grown films did not respond as well and in some cases the resistivity actually increased. Often the H can be thought to act as a defect passivation agent or as a donor [40], however, this study provides evidence against the latter case seeing as the carrier concentration went down for the films on GaAs that were annealed in H thus intensifying the debate. A more systematic study of the effects of H on ZnO grown on GaAs substrates where all of the process parameters involved are varied in a controlled manner could be in order to see if perhaps the GaAs played a role in counteracting the normally beneficial properties of H.

In this work a few test films were grown on glass substrates to verify the ellipsometry modelling even though it is an underlying assumption of this work that the films' properties will not be the same on different substrates. However, these tests were necessary to check the ellipsometry modelling because ellipsometry is not a direct measurement of film properties but rather one that requires fitting the uninteresting measured quantities  $\psi$  and  $\Delta$  to a more useful model and calculating the interesting film properties thereafter. Should the modelling procedure find a physically viable solution, it is a very powerful tool for determining the optical properties but almost always requires corroboration with other measurements making it less user-friendly. The fits performed in this study all provided physically realistic solutions and matched well with the other measurements used to verify the model. However, uncertainty still exists because the spectral range where measurements were taken did not span

the band gap of the material but rather just caught the tail edge of the onset of absorption making that particular fit parameter ( $E_g$  in the Tauc-Lorentz oscillator) not as confident as it could be if a wider range were possible.

## REFERENCES CITED

- [1] A.P. Rambu and G.I. Rusu. Effect of preparation conditions on the microstructural characteristics and optical properties of oxidized zinc films. *Superlattices and Microstructures*, **47**(2):300–307, 2010.
- [2] Yu Jin Park, Hyuk Nyun Kim, and Hyun Ho Shin. Effects of deposition temperature on the crystallinity of Ga-doped ZnO thin films on glass substrates prepared by sputtering method. *Appl. Sur. Sci.*, **255**(17):7532–7536, 2009.
- [3] Byeong-Yun Oh et al. Transparent conductive ZnO:Al films grown by atomic layer deposition for Si-wire-based solar cells. *Current Appl. Phys.*, **12**(1):273–279, 2012.
- [4] Tadatsugu Minami. Transparent conducting oxide semiconductors for transparent electrodes. *Semiconductor Science and Technology*, 20(4):S35, 2005.
- [5] Tadatsugu Minami. Present status of transparent conducting oxide thin-film development for indium-tin-oxide (ito) substitutes. *Thin Solid Films*, **516**(17):5822–5828, 2008.
- [6] Akio Suzuki, Tatsuhiko Matsushita, Takanori Aoki, Yoshitaka Yoneyama, and Masahiro Okuda. Pulsed laser deposition of transparent conducting indium tin oxide films in magnetic field perpendicular to plume. *Japanese Journal of Applied Physics*, **40**(Part 2, No. 4B):L401–L403, 2001.
- [7] Wolfram|Alpha, April, 2012. URL <http://www.wolframalpha.com/input/?i=zinc+price+compared+to+indium+price+in+US+dollars+per+gram>.
- [8] Jefferson Lab. It’s Elemental – The Periodic Table of Elements, April, 2012. URL <http://education.jlab.org/itselemental/index.html>.
- [9] Stefan Zollner. Optical constants and critical-point parameters of GaAs from 0.73 to 6.60 eV. *J. Appl. Phys.*, **90**:515, 2001.
- [10] Frederick Wooten. *Optical Properties of Solids*. Academic Press, 1972.
- [11] A. V. Singh, R. M. Mehra, Nuttawuth Buthrath, Akihiro Wakahara, and Akira Yoshida. Highly conductive and transparent aluminum-doped zinc oxide thin films prepared by pulsed laser deposition in oxygen ambient. *Journal of Applied Physics*, 90(11):5661–5665, 2001.

- [12] Norwegian University of Science and Technology. Nanordsun, May, 2012. URL <http://www.iet.ntnu.no/projects/nanordsun/>.
- [13] P. R. Willmott. Pulsed Laser Vaporization and Deposition. *Rev. of Modern Phys.*, **72**(1):315–329, 2000.
- [14] D. J. Griffiths. *Introduction to Electrodynamics*. Prentice Hall, 1999.
- [15] Center for Advanced Friction Studies. Surfaces and Contact Mechanics, April, 2000. URL [http://frictioncenter.engr.siu.edu/FS/index.php?option=com\\_content&view=article&id=71&Itemid=76](http://frictioncenter.engr.siu.edu/FS/index.php?option=com_content&view=article&id=71&Itemid=76).
- [16] Joel Duenow. *Dopants and Transport Properties of Transparent Conducting Zinc Oxide Thin Films*. PhD thesis, Colorado School of Mines, 2008.
- [17] D. L. Smith. *Thin-Film Deposition: Principles and Practice*. McGraw-Hill Professional, 1st edition, 1995.
- [18] J A Venables, G D T Spiller, and M Hanbucken. Nucleation and growth of thin films. *Reports on Progress in Physics*, **47**(4):399, 1984.
- [19] Heidi Van den Rul et al. Water-based wet chemical synthesis of (doped) ZnO nanostructures. *J. Sol-Gel Sci. Techn.*, **39**:41–47, 2006.
- [20] M. Ohyama, H. Kouzuka, and T. Yoko. Sol-gel preparation of ZnO films with extremely preferred orientation along (002) plane from zinc acetate solution. *Thin Solid Films*, **306**(1):78–85, 1997.
- [21] Y. Zang, Z. Zhang, B. Lin, Z. Fu, and J. Xu. Effects of Ag doping on the photoluminescence of ZnO films grown on Si substrates. *J. Phys. Chem. B*, **109**:19200–19203, 2005.
- [22] J. Lee, K. Ko, and B. Park. Electrical and optical properties of ZnO transparent conducting films by the sol-gel method. *J. Crystal Growth*, **247**:119–125, 2003.
- [23] P.-C. Yao et al. Optical and electrical characteristics of Al-doped ZnO thin films prepared by aqueous phase deposition. *Appl. Surface Sci.*, **257**:1441–1448, 2010.
- [24] P. Sagar, M. Kumar, and R. M. Mehra. Influence of hydrogen incorporation in sol-gel derived aluminum doped ZnO thin films. *Thin Solid Films*, **489**:94–98, 2005.
- [25] S. M. Sze. *Semiconductor Physics*. John Wiley and Sons, 2 edition, 2002.

- [26] J. G. Lu, Z. Z. Ye, Y. J. Zeng, L. P. Zhu, L. Wang, J. Yuan, B. H. Zhao, and Q. L. Liang. Structural, optical, and electrical properties of (Zn,Al)O films over a wide range of compositions. *JOURNAL OF APPLIED PHYSICS*, 100(7):073741, 2006.
- [27] K Ellmer. Resistivity of polycrystalline zinc oxide films: current status and physical limit. *Journal of Physics D: Applied Physics*, 34(21):3097, 2001.
- [28] P. Gondoni, M. Ghidelli, F. Di Fonzo, V. Russo, P. Bruno, J. Mart-Rujas, C.E. Bottani, A. Li Bassi, and C.S. Casari. Structural and functional properties of al:zno thin films grown by pulsed laser deposition at room temperature. *Thin Solid Films*, (0):1 – 12, 2011.
- [29] Donald A. Neaman. *Semiconductor Physics and Devices*. McGraw–Hill, 4th edition, 2012.
- [30] L. J. van der Pauw. A method of measuring specific resistivity and hall effect of disks of arbitrary shape. *Phillips Res. Repts*, **13**(1):1–9, 1958.
- [31] Ji-Myon Lee et al. Low-resistance and nonalloyed ohmic contacts to plasma treated ZnO. *Appl. Phys. Lett.*, **78**(24):3842–3844, 2001.
- [32] K. Ip et al. Carrier concentration dependence of Ti/Al/Pt/Au contact resistance on n-type ZnO. *Appl. Phys. Lett.*, **84**(4):544–546, 2004.
- [33] Han-Ki Kim et al. Electrical and interfacial properties of nonalloyed Ti/Au ohmic and Pt Schottky contacts on Zn-terminated ZnO. *Jap. J. of Appl. Phys.*, **41**(3A):1560–1565, 2006.
- [34] Han-Ki Kim et al. Low-resistance Ti/Au ohmic contacts to Al-doped ZnO layers. *Appl. Phys. Lett.*, **77**(11):1647–1649, 2000.
- [35] Toshimitsu Akane, Koji Sugioka, and Katsumi Midorikawa. Nonalloy Ohmic contact fabrication in a hydrothermally grown n-ZnO (0001) substrate by KrF excimer laser irradiation. *J. Vac. Sci. Technol. B*, **18**(3):1406–1408, 2000.
- [36] J. Peisner, P. Roboz, and P. B. Barna. Thickness dependence of the quantum yield and attenuation length of photoelectrons in thin indium films. *Phys. Stat. Sol. A*, **4**(3):K187–K191, 1971.
- [37] K. Jacobi, G. Zwicker, and A. Gutmann. Work function, electron affinity, and band bending of zinc oxide surfaces. *Surface Science*, **141**:109–125, 1984.
- [38] J. A. Woollam Co. Guide to using WVASE32.

- [39] Stefan Zollner. Model dielectric functions for native oxides on compound semiconductors. *Appl. Phys. Lett.*, **63**:2523, 1993.
- [40] Chris G. Van de Walle. Hydrogen as a cause of doping in zinc oxide. *Phys. Rev. Lett.*, **85**:1012–1015, 2000.
- [41] P. D. C. King and T. D. Veal. Conductivity in transparent oxide semiconductors. *J. Phys - Condens. Mat.*, **23**(33):334214, 2011.
- [42] Deok-Yong Cho, Jeong Hwan Kim, and Cheol Seong Hwang. Electron hopping interactions in amorphous ZnO films probed by x-ray absorption near edge structure analysis. *Appl. Phys. Lett.*, **98**(22):222108, 2011.
- [43] J. R. Bellingham, W. A. Phillips, and C. J. Adkins. Intrinsic performance limits in transparent conducting oxides. *Journal of Materials Science Letters*, 11:263–265, 1992.
- [44] Klaus Ellmer and Rainald Mientus. Carrier transport in polycrystalline transparent conductive oxides: A comparative study of zinc oxide and indium oxide. *Thin Solid Films*, 516(14):4620–4627, 2008.
- [45] Klaus Ellmer and Rainald Mientus. Carrier transport in polycrystalline ito and zno:al ii: The influence of grain barriers and boundaries. *Thin Solid Films*, 516(17):5829 – 5835, 2008.
- [46] M.A. Martinez, J. Herrero, and M.T. Gutierrez. Properties of rf sputtered zinc oxide based thin films made from different targets. *Solar Energy Materials and Solar Cells*, **31**(4):489 – 498, 1994.
- [47] Yasuhiro Igasaki and Hiromi Saito. Substrate temperature dependence of electrical properties of zno:al epitaxial films on sapphire (12-bar 10). *J. Appl. Phys.*, **69**(4): 2190–2195, 1991.
- [48] Ocal Tuna, Yusuf Selamet, Gulnur Aygun, and Lutfi Ozyuzer. High quality ito thin films grown by dc and rf sputtering without oxygen. *Journal of Physics D: Applied Physics*, **43**(5):055402, 2010.
- [49] H Agura, A Suzuki, T Matsushita, T Aoki, and M Okuda. Low resistivity transparent conducting Al-doped ZnO films prepared by pulsed laser deposition. *THIN SOLID FILMS*, **445**(2):263–267, 2003.
- [50] Anderson Janotti. Defects and doping in oxides: What we have learned so far. URL <http://www.stanford.edu/group/nnin-computing/talks/A.Janotti.pdf>.

- [51] A. Sarkar, S. Ghosh, S. Chaudhuri, and A.K. Pal. Studies on electron transport properties and the burstein-moss shift in indium-doped zno films. *Thin Solid Films*, **204**(2): 255 – 264, 1991.
- [52] J. Clatot, G. Campet, A. Zeinert, C. Labrugre, and A. Rougier. Room temperature transparent conducting oxides based on zinc oxide thin films. *Applied Surface Science*, **257**(12):5181 – 5184, 2011.
- [53] J. I. Langford and A. J. C. Wilson. Scherrer after sixty years: A survey and some new results in the determination of crystallite size. *Journal of Applied Crystallography*, **11**(2):102–113, 1978.
- [54] I. Sieber, N. Wanderka, I. Urban, I. Drfel, E. Schierhorn, F. Fenske, and W. Fuhs. Electron microscopic characterization of reactively sputtered zno films with different al-doping levels. *Thin Solid Films*, **330**(2):108 – 113, 1998.
- [55] Satoru Yoshioka, Fumiyasu Oba, Rong Huang, Isao Tanaka, Teruyasu Mizoguchi, and Tomoyuki Yamamoto. Atomic structures of supersaturated zno–al<sub>2</sub>o<sub>3</sub> solid solutions. *Journal of Applied Physics*, **103**(1):014309, 2008.
- [56] Satoru Yoshioka, Kazuaki Toyoura, Fumiyasu Oba, Akihide Kuwabara, Katsuyuki Matsunaga, and Isao Tanaka. First-principles investigation of r<sub>2</sub>o<sub>3</sub>(zno)<sub>3</sub> (r=al, ga, and in) in homologous series of compounds. *Journal of Solid State Chemistry*, **181**(1):137–142, 2008.
- [57] R. G. Hunsperger, R. G. Wilson, and D. M. Jamba. Mg and Be Ion Implanted GaAs. *J. Appl. Phys.*, **43**(3):1318–1320, 1972.

## APPENDIX - ELLIPSOMETRY MODELING AND PARAMETERS

Ellipsometric measurements were taken using a rotating analyzer with a scanning monochromatic light source. Clear tape was placed on the back of the wafer and over the front of the wafer where there was no film. Figure 2.3 shows the area of the film on the sample substrate. Everywhere that the shadow mask blocked, I placed tape in order to eliminate any signal coming from the exposed GaAs substrate. Typical parameters used for fitting the ellipsometry model are given in Table Table A.1.

Table A.1: Summary of the parameters used to model the optimal film.

A	109.93
En	9.2695
C	18.552
Eg	2.7251
N	4.65E+20
mu	27.72
m*	0.39
MSE	5.842

Figure A.1 shows the measured and fit results for the optimised film with an MSE of 5.8.

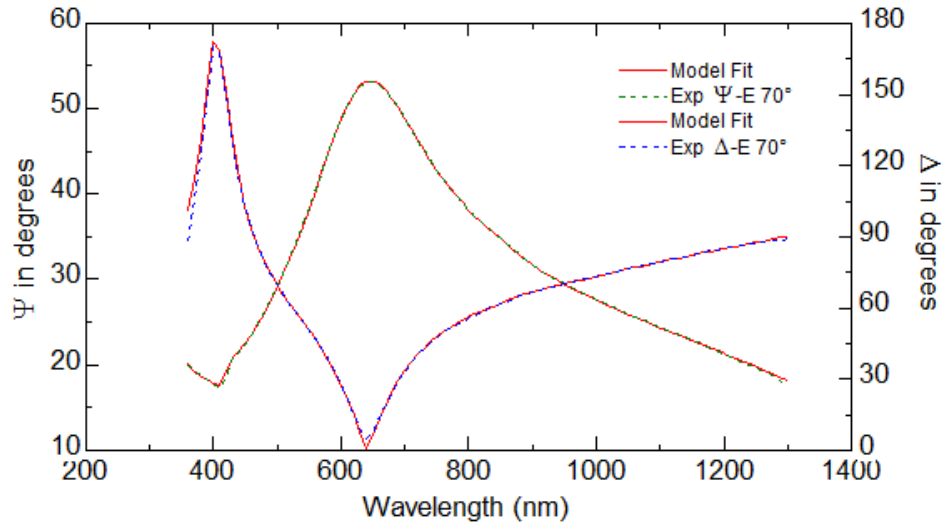


Figure A.1: Typical ellipsometry fitting results for Psi and Del of the optimised film.